

MSCI PROJECT SUBMISSION TO THE DEPARTMENT OF PHYSICS AND ASTRONOMY  
UNIVERSITY COLLEGE LONDON - PHYSICS

# **Investigating Ionospheric Plasma Drifts and Thermospheric Neutral Winds Using CubeSats**

**Rifat Mahammod**

**1st Supervisor: Dr. Anasuya Aruliah**  
**2nd Supervisor: Prof. Dhiren Kataria**



**Submission of coursework for Physics and Astronomy course PHAS0097/PHAS0048  
2020/21**

Please sign, date and return this form with your coursework by the specified deadline.

**DECLARATION OF OWNERSHIP**

I confirm that I have read and understood the guidelines on plagiarism, that I understand the meaning of plagiarism and that I may be penalised for submitting work that has been plagiarised.

I confirm that all work will also be submitted electronically and that this can be checked using the JISC detection service, Turnitin®.

I declare that all material presented in the accompanying work is entirely my own work except where explicitly and individually indicated and that all sources used in its preparation and all quotations are clearly cited.

Should this statement prove to be untrue, I recognise the right of the Board of Examiners to recommend what action should be taken in line with UCL's regulations.

Signed

A handwritten signature in black ink, appearing to read 'Rifat Mahamood'.

PrintName

RIFAT MAHAMOOD

Dated

12/04/2021

Title	Date Received	Examiner	Examiner's Signature	Mark

## **Abstract**

The thermosphere is a layer of the atmosphere that is scarce in observations. Phoenix, from the QB50 mission, was one of the Cubesats that collected oxygen ( $O_+$ ) counts via an Ion and Neutral Mass Spectrometer (INMS), with the aim of exploring the thermosphere in more depth. The aim of this project is to calculate the calibration factor and the thermospheric neutral wind speed with the aid of a model that I derived, which takes into account INMS counts and oxygen number densities. Using empirical models such as the Horizontal Wind Model and the International Reference Ionosphere, I have visually evaluated a possible relationship between the collected INMS counts and the neutral wind speeds. The resulting calibration factor and neutral wind speed were estimated to be  $9.59 \times 10^5$  and  $6732.2 ms^{-1}$ , respectively. To explain the discrepancy in the neutral wind speed, future research should focus on implementing relevant attitude control systems for more accurate data collection.

---

## Contents

<b>1 Glossary</b>	<b>2</b>
<b>2 Introduction</b>	<b>3</b>
<b>3 Background</b>	<b>4</b>
3.1 The Thermosphere	4
3.2 Thermospheric Density	5
3.3 Thermospheric winds	7
<b>4 Method</b>	<b>8</b>
4.1 Current Observation Techniques	8
4.2 Theoretical and Empirical Models	9
4.2.1 Horizontal Wind Model	9
4.2.2 International Reference Ionosphere	9
4.2.3 NRLMSISE Model	10
4.3 QB50 CubeSat mission	10
4.3.1 Ion and Neutral Mass Spectrometer	11
4.3.2 Measurements from Phoenix	11
4.3.3 INMS Data	12
4.4 Project Methodology	13
4.4.1 Textfiles Data	13
4.4.2 INMS Data Visualization	15
4.4.3 Deriving The Wind Speed Model	17
4.4.4 Graphs and Plots	19
<b>5 Results and Analysis</b>	<b>22</b>
5.1 Simultaneous Equations Method	22
5.2 Clustering Data	23

5.3	Day and Night Subplots	24
5.3.1	INMS counts Subplots	24
5.3.2	HWM and NRLMSISE Subplots	25
5.4	HWM Vector Fields	27
5.5	Comparing Vector Fields and Full Run INMS Counts	32
5.6	IRI O+ Density Model	32
5.7	Calculating the Calibration Factor and The Wind Velocity	34
5.8	Discussion	36
<b>6</b>	<b>Conclusion</b>	<b>37</b>
<b>A</b>	<b>Appendix</b>	<b>41</b>
A.1	Python Data Cleaning Script	41
A.2	MATLAB Code for Plotting Gaussian To Full Run INMS Counts	42
A.3	MATLAB Code for The HWM Vector Fields	43
A.4	MATLAB Code for NRLMSISE Oxygen Densities Along Phoenix Path	44
A.5	MATLAB Code for HWM Wind Speed Along Phoenix Path	45
A.6	MATLAB Code for HWM Vector Fields overlaid on NRLMSISE Contour Maps	47
A.7	Calculations of Angle Between HWM Vectors and INMS's Look Direction	48
A.8	Final Calculation of Calibration Factor and Neutral Wind Speed	49
A.9	Pitch Angle Distribution	50

---

## 1 Glossary

Ion and Neutral Mass Spectrometer	INMS
Horizontal Wind Model	HWM
International Reference Ionosphere	IRI
US Naval Research Laboratory Mass Spectrometer and Incoherent Scatter Radar	NRLMSISE
High Geometric Factor	HGF
Extreme Ultraviolet	EUV

## 2 Introduction

The atmosphere of the Earth is composed of a mix of stratified gaseous layers. Retained by gravity, the atmosphere surrounds the entire planet, providing the earth with sustained life through optimal solar heating and suitable air composition. Without this protective blanket of gas, the severe conditions caused by the solar system would make the Earth an inhabitable place. Beyond the basic survival needs, the atmosphere has physical and optical properties that can be employed for continuous technological advancements, such as telecommunication and earth observation.

The Earth's atmosphere is divided into the troposphere, stratosphere, mesosphere, thermosphere and exosphere. From the ground to the outermost layer, this mix of gaseous envelopes encompasses a variety of unexplored regions. Due to this scarcity of atmospheric observations, the demand for new atmospheric research methodologies has steadily increased over time [1]. Although, advancements in this field have been characterized by continuous obstacles caused by the physical and chemical complexity of the atmosphere, improvements to ground-based measurement techniques and satellite-borne instruments have facilitated significantly global weather and climate coverage. As observational capabilities are expanded, empirical models are required to be frequently updated as changes in atmospheric properties need to be incorporated. These periodic adjustments are vital as they provide precise mechanisms to study space weather, satellite drag and the relationship between lower and upper atmosphere [2].

The demand for improved observational capacity is what motivates this paper, as it aims to describe the methods with which CubeSats can be utilised to enhance measurement techniques of the upper atmosphere. These nano-satellites, with a weight of no more than 3kg and dimensions of a  $10\text{cm}^3$  cube, were invented with the scope of collecting accurate in-situ data, as remote sensing measurements become unfeasible due to the rarefied thermospheric air. The QB50 mission, consisting of 36 CubeSats, was launched to collect multi-point in situ measurements of the lower thermosphere. Each satellite was equipped with a data collection instrument capable of gathering data of a particular property of the thermosphere. The Phoenix CubeSat, fitted with the an Ion and Neutral Mass Spectrometer (INMS), has

collected particles counts data, which is going to be analysed and evaluated in this paper.

The overall purpose of the project is to contribute towards the wider long-term goal of investigating new and innovative ways to measure atmospheric parameters using in-situ data collected by CubeSats. The aim of this project is to calculate the thermospheric wind speeds of atomic oxygen with the aid of a model derived from the INMS peak count with respect to Phoenix's pitching angle. By investigating the relationship between INMS counts and oxygen number densities a calibration factor will be obtained. Visual interpretations of empirical models such as the Horizontal Wind Model (HWM) and the International Reference Ionosphere (IRI) will be suggested in order to find a correlation between the wind directions and the INMS counts. With the outcome of this project, this report hopes to provide more methodologies to access research data from regions of the atmosphere that are currently poorly understood.

### 3 Background

#### 3.1 The Thermosphere

The thermosphere, which extends from about 85 to 500 km [3], is the layer of the atmosphere that divides the lower atmosphere from the upper atmosphere, acting as an imaginary boundary which separates the Earth from outer space. The temperature of this region generally increases as a function of height, as shown in figure 1. It can drastically vary from 500K to 2000K depending on solar flux and geomagnetic activity [3]. The main cooling mechanisms involve heat dissipation to space through infrared radiation and downward molecular heat propagation [3].

The lower thermosphere is composed by heavier molecules such as  $O_2$  and  $N_2$ . As altitude increases, the density of heavy components decreases and the chemical distribution of the upper thermosphere becomes increasingly populated with atomic oxygen  $O$  and atomic nitrogen  $N$ . Extreme ultraviolet (EUV) light emitted from the sun interacts with molecules such as ozone  $O_3$  [3]. Via the process of photodissociation, heavier components are decomposed to form lighter constituents such as  $O$  [3]. In addition, highly energetic solar radiation leads to intense photo-ionization of neutral atoms, producing electrically charged particles

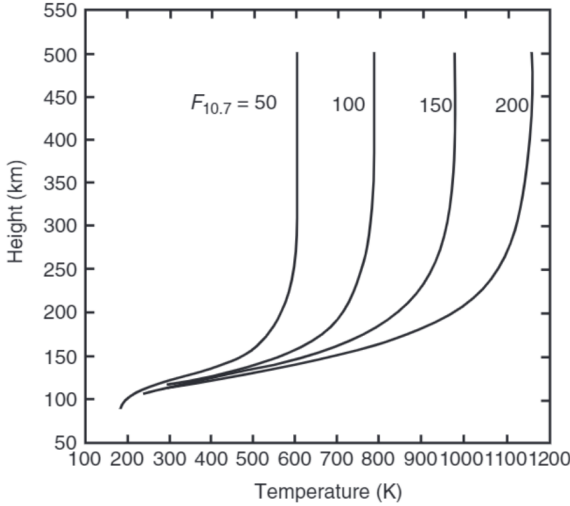


**Figure 1:** Diagram showing the temperature profile of the thermosphere as a function of altitude, as it varies with respect to the F10.7cm solar flux index [3].

and free electrons that make up the ionosphere. This layer encompasses the entire thermosphere, as demonstrated in figure 2. The interactions between neutral and ionic particles are highly responsible for the various dynamic processes arising in the upper atmosphere.

### 3.2 Thermospheric Density

Following an exponential drop in neutral density, as demonstrated in figure 2, the atmosphere changes from a molecular atmosphere to an atomic atmosphere. The density of neutral particles drops as the height from the ground increases. In the upper atmosphere the air becomes so thin that fluid dynamics becomes obsolete for physical modelling and predictions [23]. Above an altitude of 400km, the reduced particle density allows satellite orbits and space-craft missions to experience a modest drag force.

The global mean density of the thermosphere fluctuates because of a large variation in the EUV radiation with respect to the time of the day. Due to the variability in solar radiation at a given time, diurnal and seasonal variations are responsible for differences in density at a particular height. As EUV radiation heats up the upper atmosphere during the day, the denser air situated in the lower part of the thermosphere expands upwards due to the increased thermal energy, causing neutral densities to increase at a given height [5]. The

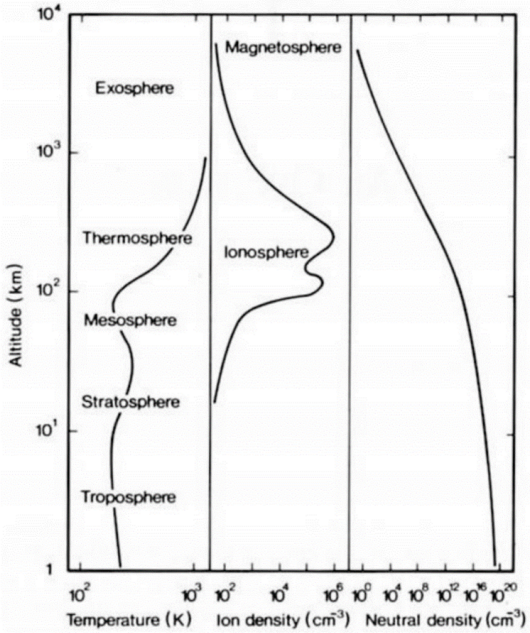


**Figure 2:** Diagram showing subplots of a temperature profile, ionic density and neutral density of the atmosphere, all with respect to altitude [4].

density of plasma produced via ionization of neutral gases, also fluctuates with respect to altitude as changes in EUV radiation causes the size of the ionosphere to vary depending on the time of the day [6]

In addition to diurnal changes in solar radiation, thermospheric densities are also influenced by periodic fluctuations in solar activity. Solar EUV radiation is tracked via the F10.7cm radio flux emissions, which can be represented as a measure of solar activity as it correlates well with the number of sunspots. A complete solar cycle consists of approximately 11 years of fluctuations between solar minimum and maximum. During a period of high solar activity, highly energetic solar particles interact with the thermosphere, increasing neutral and ionic densities. The opposite is demonstrated in figure 3 [7], which shows that the 2008 solar minimum has observed a 3.7% decrease in solar activity, which corresponded to a 28% decrease in atmospheric density.

Thermospheric densities are also influenced by changes in geomagnetic activity, which measures disturbances in the Earth's horizontal component of the magnetic field. The strength of the geomagnetic activity is described by the  $k_p$  and  $a_p$  indices. Interactions of the solar

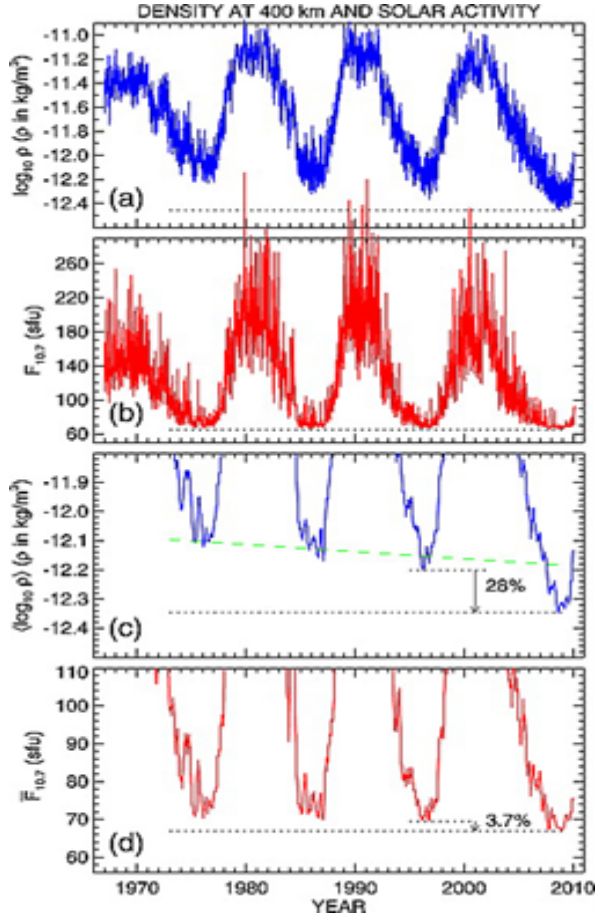


**Figure 3:** (a) Daily global-average mass log density. (b) The daily F10.7 cm solar radio flux. (c) Running 81-day average log-densities. (d) Showing the 81-day average of F10.7 cm solar radio [7].

wind with the magnetic field of the earth can produce momentary disruptions which can cause thermospheric densities to increase, as the upper atmosphere undergoes expansion due to Joule Heating [8].

### 3.3 Thermospheric winds

The main factor responsible for the thermospheric circulation is the temperature gradient between the day side and night side thermosphere. The vertical expansion of air caused by EUV radiation creates large horizontal pressure gradients, giving rise to the thermospheric horizontal wind field. The predominant forces that drive these winds include gravity, solar flux, tides, ion-neutral collisions, molecular viscosity and ion drag force. While the Coriolis

force can be neglected in the upper thermosphere, the general wind pattern is determined by a balance between the pressure gradients due to solar heating and the ion drag force [3]. Since the ion drag force arises from ion-neutral collisions, the wind in the mid-latitude thermosphere sees lower magnitudes during the day, due to increased ion drag forces from large electron densities. At night, however, ion drag drops due to recombination of electrons, giving rise to greater neutral wind speeds. At higher latitudes, ion drifts generated by electric fields in the auroral region drive larger neutral winds due to more frequent ion-neutral momentum exchange [3]. Ionospheric plasma drifts and thermospheric neutral winds, therefore, mirror the same general pattern around the polar region.

## 4 Method

This section of the report is going to introduce some of the observational techniques used for atmospheric research. The role and the usefulness of theoretical and empirical models is going to be discussed. Finally, the novel methodology of using CubeSats with fitted Ion Neutral Mass Spectrometers (INMS) is going to be presented and described in details.

### 4.1 Current Observation Techniques

Traditional observation techniques of the lower-middle thermosphere involve three main approaches. Fabri-Perot Interferometers (FPI) and Incoherent Scatter Radars observations involve the use of ground-based remote sensing techniques. Satellite drag-based calculations, instead, uses in-situ data to calculate local density measurements [13].

FPIs are able to build a picture of the thermosphere by monitoring the airglow at an altitude of around 200 to 300km. Doppler shift of line emissions, which occur due to atomic excitation in the thermosphere, can help retrieve useful thermospheric information [9]. As neutral particles move with excited atoms, measurements of neutral temperatures and wind velocities can be calculated remotely using FPIs. The main disadvantage of FPIs is due to the fact that the accuracy of the measurements are highly dependent on optimal weather conditions such as dark clear skies.

Satellite drag-based calculations utilizes on board accelerometers to obtain density measurements. Satellites such as the Challenging Mini-satellite Payload (CHAMP) obtains drag coefficient measurements from its own velocity and trajectory. Although accelerometers are able to quantify thermospheric parameters such as density, neutral winds and temperature [10], the data collected is highly localised, which cannot be extrapolated to global scales.

## 4.2 Theoretical and Empirical Models

Theoretical models predict the state of the atmosphere purely based on physics-based calculations. These models behave according to physical laws of fluid dynamics, such as the Navier-Stokes equation and the continuity equation. Examples of theoretical models include the General Circulation Model (GCM) and the Global Ionosphere-Thermosphere Model (GITM). Empirical models, instead, incorporates observations into the simulations, in order to improve predictions of a range of different atmospheric variables. Examples of empirical models consist of NRLMSISE-00, IRI and HWM.

### 4.2.1 Horizontal Wind Model

The Horizontal Wind Model (HWM) is an empirical model able to compute the horizontal vector wind fields of the atmosphere, from sea level to about 450km [10]. The model takes into account all the physical factors that affect thermospheric variables, which were described in section 3.2 and 3.3. The HWM is refined by integrating ground-based observations collected by FPIs and incoherent scatter radars. The new upgrade of the HWM also incorporates observations of cross-track winds gathered via satellites such as the GOCE satellite [11]. In this project, calculations using the HWM were performed using an in-built MATLAB function which is part of the Aerospace Toolbox. This function takes in parameters such as spatial coordinates, time, date and  $A_p$  index and outputs a vector whose components consist of meridional and zonal winds.

### 4.2.2 International Reference Ionosphere

The International Reference Ionosphere (IRI) model is an empirical and climatic model which describes the ionic densities and temperatures of the Ionosphere. The model, which

ranges from 50km to approximately 2000km, is periodically updated to reflect observational changes recorded by ground-based instruments and orbiting satellites [12]. Although IRI produces electron density results that are only monthly averages, it provides a reference framework for other models, such as the HWM, to rely on. In this project, the IRI model is computed through a website which calculates electron density and ionic compositions based on date, time and spatial coordinates. Since IRI only relies on observations made from local ionosondes, the model tends to have a low accuracy on a global scale [12].

#### 4.2.3 NRLMSISE Model

The US Naval Research Laboratory Mass Spectrometer and Incoherent Scatter Radar (NRLMSISE) is another empirical model, which aims to compute neutral temperatures and densities of the atmosphere. Ranging from sea level to about 500km in altitude, the NRLMSISE is primarily based on observational data from incoherent scatter radars and satellite drag data. Despite the model being susceptible to changes in geomagnetic activity and variation in solar radiation, global NRLMSISE predictions are obtained through statistical averages from local observations [1]. The project involves the use of this model through a MATLAB in-built function from the Aerospace Toolbox, which allows the calculation of neutral oxygen densities.

### 4.3 QB50 CubeSat mission

Ground-based measurements have always been limited by the complexity of the overall atmosphere. As orbiting satellites can only collect data from the upper thermosphere, the Lower Thermosphere-Ionosphere (LTI) represents the region that is commonly known as the "ignorosphere", due to the shortage of in-situ data [13]. In 2017, the QB50 project was launched by university teams across the world, with the intention of making earth observation and space missions more affordable and sustainable. The Phoenix CubeSat was developed by the National Cheng Kung University, in Taiwan. Phoenix weighted less than 2kg and had dimensions of  $10 \times 10 \times 20 \text{ cm}^3$ . It was fitted with an Ion and Neutral Mass Spectrometer (INMS), which recorded the count number of a range of neutral and ionic particles [14].

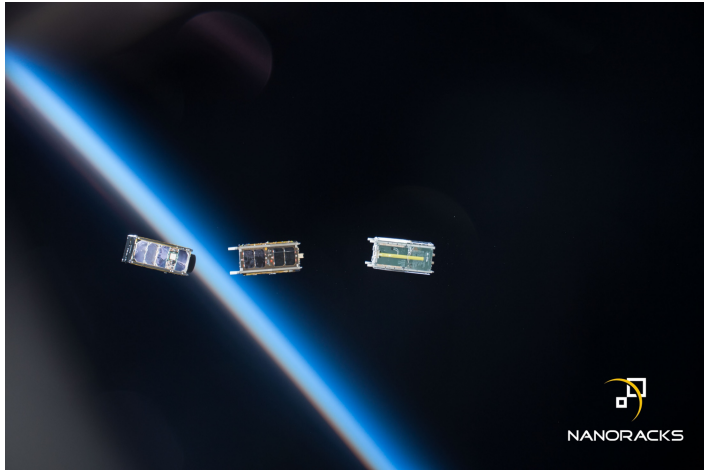


**Figure 4:** CubeSats orbiting the earth shortly after the launch from the International Space Station [16].

#### 4.3.1 Ion and Neutral Mass Spectrometer

The INMS is a remote sensing instrument capable of determining the chemical composition of a gas sample. The theory behind the INMS is based on the principle of mass spectrometry. At first, the gaseous ions enter the equipment through an aperture which leads to the acceleration phase where an electric field produced by two oppositely charged plates accelerate the ions to an optimal velocity before they enter the deflection chamber. In this phase, the positively charged ions are deflected by a magnetic field produced via an electromagnet. The amount of deflection a particle is subjected to, depends on the mass to charge ratio of the particle. Only ions with the desired mass-to-charge ( $m/z$ ) ratio are able to reach the detector. Varying the electromagnet's voltage allows to scan through different  $m/z$  values, in order to select an accurate mass spectrum for the gaseous sample [20]. The diagram in figure 5 shows a simplified illustration of the INMS.

#### 4.3.2 Measurements from Phoenix

Phoenix's INMS was set to collect count numbers of ionised oxygen ( $O^+$ ) at specific times and locations. The data was gathered by the INMS in the following way. At first, energy sweeps of 16 voltage steps are carried out in order to scan for oxygen particles. As the voltage changes from low to high, the number of counts for each step is recorded by the

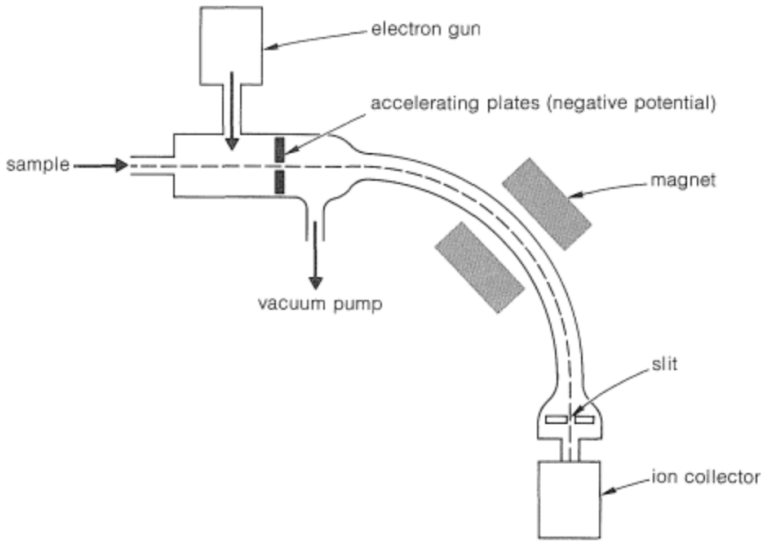


**Figure 5:** Simple diagram of the INMS. Labels show the different chambers and phases [15].

INMS. An example of an energy profile of these sweeps is shown in figure 6, which was created by Dhiren Kataria [21]. The total acquired data from these sweeps can be divided into two categories. The first category is based on data collected via a high geometric factor (HGF). These are the counts that were recorded through larger apertures in the INMS. As each 16 steps energy sweep take 10ms, HGF data contributes to a higher resolution of counts. The counts in the second category belongs to the low geometric factor data. Smaller INMS apertures are used to make these measurements and each energy sweep takes 20ms to take place, which leads to a smaller number of counts per second. With 60 packets of data collected, the HGF run time is estimated to be 2.88 minutes. Since, 180 packets of low geometric factor data contributes to a run time of 17.88 minutes, the total INMS run time for each day is estimated to be approximately 22 minutes.

#### 4.3.3 INMS Data

The data counts from the energy sweeps were first stored in bytes, in raw files with ".dat" extension. These were then extracted into readable formats from the original data packets that were made available by the MSSL [17]. As demonstrated in figure 6, the number of counts form Gaussian distributions about the peak value of 4.90eV, which is located at the red

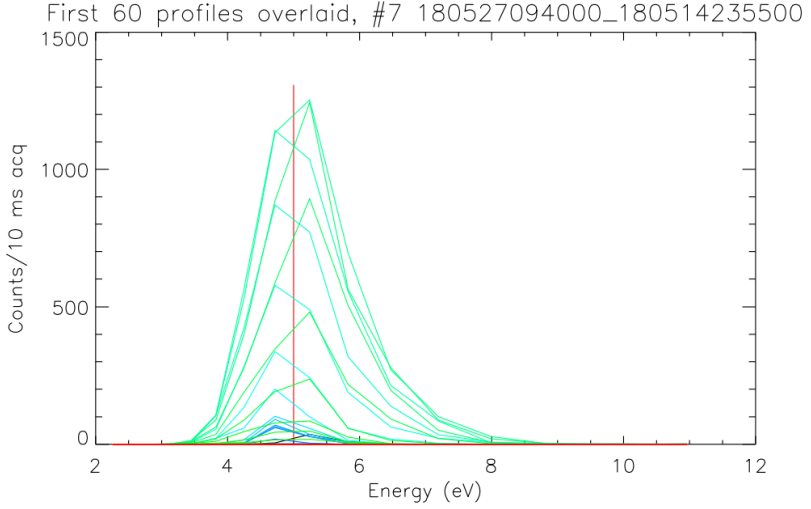


**Figure 6:** High geometric factor energy profile for the 27th of May 2018. The horizontal axis shows the voltage sweeps going from 2eV to 12eV, while the vertical axis shows the number of counts for each voltage sweep.

vertical line. As this corresponds to the energy of an oxygen particle ( $O^+$ ), maximum count values from these Gaussian distributions were finally extracted into textfiles by a previous UCL student named Ali Ozkidir [16]. These are illustrated in the last column of the example textfile in figure 7, which is a screenshot of the data collected on the 19th of May 2018. Hence the counts in the textfiles from each different date represent oxygen ( $O^+$ ) readings collected by the INMS. In this report, textfiles from specific dates are analysed through visual plots and graphs in order to explain patterns and cross validate density results with various empirical models, with the potential aim of calculating thermospheric neutral wind speeds.

## 4.4 Project Methodology

### 4.4.1 Textfiles Data

The data available for the completion of this project comprised of a folder containing 29 different textfiles. As illustrated by the example in figure 7 and described in section 4.3.3, these textfiles correspond to the INMS data gathered on 29 different dates, between May and July 2018. The first step taken in this project involved the use of MATLAB to extract the time

2018-5-19 - Notepad

2018-05-19	13:35:18.020000	-65.1499	-47.3792	370.4337	36		
2018-05-19	13:35:18.240000	-65.1499	-47.3792	370.4337	0		
2018-05-19	13:35:18.580000	-65.1499	-47.3792	370.4337	0		
2018-05-19	13:35:18.980000	-65.1499	-47.3792	370.4337	56		
2018-05-19	13:35:19.200000	-65.1499	-47.3792	370.4337	0		
2018-05-19	13:35:19.540000	-65.1499	-47.3792	370.4337	0		
2018-05-19	13:35:19.940000	-65.1499	-47.3792	370.4337	78		
2018-05-19	13:35:20.160000	-65.1499	-47.3792	370.4337	0		
2018-05-19	13:35:20.500000	-65.1499	-47.3792	370.4337	0		
2018-05-19	13:35:20.900000	-65.1499	-47.3792	370.4337	81		
2018-05-19	13:35:21.120000	-65.1499	-47.3792	370.4337	0		
2018-05-19	13:35:21.460000	-65.1499	-47.3792	370.4337	0		
2018-05-19	13:35:21.860000	-65.1499	-47.3792	370.4337	64		
2018-05-19	13:35:22.080000	-65.1499	-47.3792	370.4337	0		
2018-05-19	13:35:22.420000	-65.1499	-47.3792	370.4337	0		
2018-05-19	13:35:22.820000	-65.1499	-47.3792	370.4337	67		
2018-05-19	13:35:23.040000	-65.1499	-47.3792	370.4337	0		
2018-05-19	13:35:23.380000	-65.1499	-47.3792	370.4337	0		
2018-05-19	13:35:23.980000	-65.1499	-47.3792	370.4337	71		
2018-05-19	13:35:24.200000	-65.1499	-47.3792	370.4337	0		
2018-05-19	13:35:24.540000	-65.1499	-47.3792	370.4337	0		
2018-05-19	13:35:24.940000	-65.1499	-47.3792	370.4337	91		
2018-05-19	13:35:25.160000	-65.1499	-47.3792	370.4337	0		

**Figure 7:** This is a snapshot of the available data in textfile format. The first two columns show the date and time. The next three columns show the longitude, latitude, altitude of the CubeSat. The last column is made up of the INMS counts. This specific example corresponds to the data collected by the INMS on the 19th of May 2018.

and the number of counts from the textfiles. As a form of preliminary analysis, certain dates were plotted to verify that the correct shape matched the graphs illustrated by Ali Ozkidir in his paper [17]. All the resulting plots showed a systematic error, which is demonstrated in the example plot in figure 8, by the constant horizontal array of points at around  $y = 370$ . Further inspection of the data suggested that the systematic error in all the plotted dates were due to certain columns overlapping each other, hence the altitude column being read by MATLAB as count readings. Subsequently, a data cleaning routine via a Python script was written to create new corrected textfiles for every single date. The code is shown in appendix A.1.

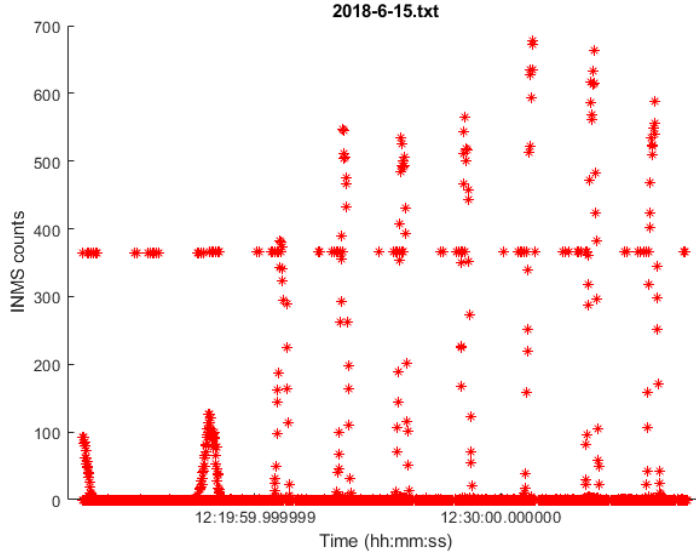


**Figure 8:** Plot of total runtime INMS counts against time for the 15th of June 2018. Graph shows data from the original textfiles before data cleaning routine was performed.

#### 4.4.2 INMS Data Visualization

The INMS counts were correctly plotted against time after the data files were cleaned and revised. After reasonably accounting for any background errors and removing zero count clutters, MATLAB's inbuilt curve fitting tool was used to fit Gaussian distributions to the data, with the code in appendix A.2. This is demonstrated by the example plot from the 28th of May 2018, shown in figure 9, where the INMS count readings in blue are fitted by the red curve. The presence of these normally distributed data points suggest that the CubeSat has been subjected to a pitching motion, as shown in figure 10. Due to the tumbling, the number of particles entering the INMS varies with time and angle, with a maximum number of counts recorded when the CubeSat directly faces the direction of motion, which drops as the INMS slowly pitches away.

The tumbling rate was calculated by first inspecting the number of peaks each day. Since the gap between each peak corresponds to a  $360^\circ$ angle, the tumbling rate can be obtained if the total rotational angle ( $360 \times 8 = 2880^\circ$ ) is divided by the total run time. This method gave a tumbling rate of 1.97 deg/s.

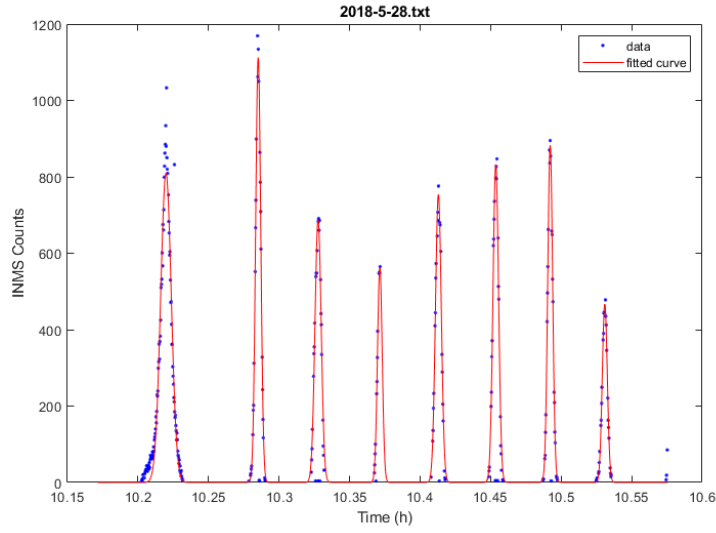


**Figure 9:** Plot of total runtime INMS counts against time for the 28th of May 2018. Graph shows data fitted by Gaussian distributions after the background and systematic errors were removed.

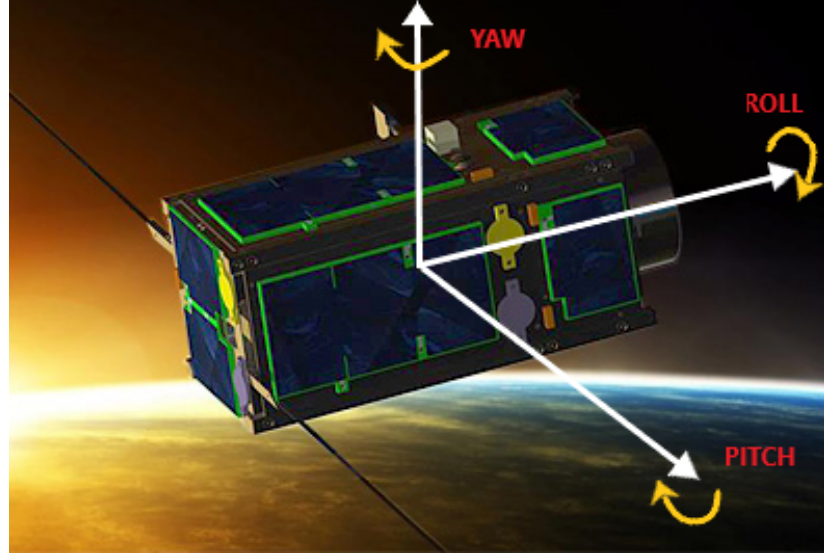


**Figure 10:** Picture of Phoenix and the different axis of rotation.

The graph illustrated in figure 9 shows 8 different peaks. The first peak contains a large amount of data points relative to the other peaks. This is because the data in the first peak represents the HGF counts. A closer look at this peak is demonstrated in figure 11. The black circles indicate attitude readings as Phoenix is pitching. These pitch data points, as shown

in figure 11, had to be extracted manually from a different dataset, as these were not readily available. These were finally fitted by the green linear plot with the aim of investigating the direction of neutral winds using the HGF INMS peaks.

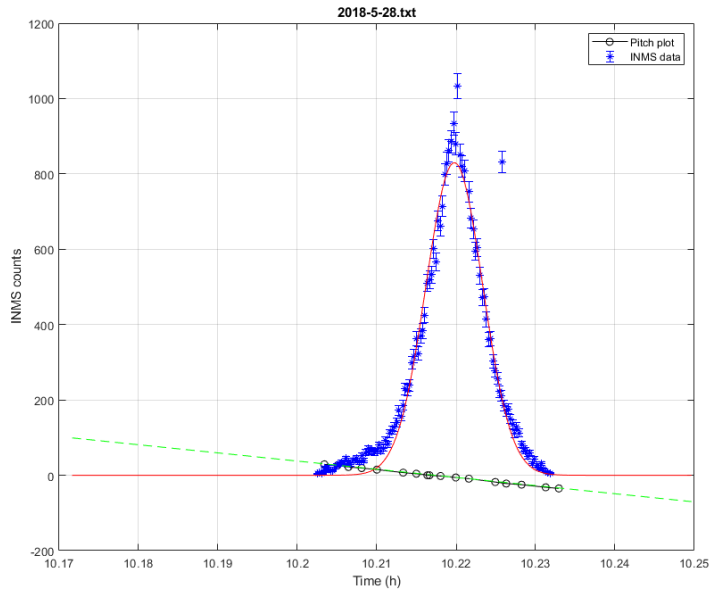


**Figure 11:** Graph of the high geometric factor peak from the data collected on the 28th of May 2018. This is the first peak from figure 9. The black pitch data are also plotted and fitted by the green line.

#### 4.4.3 Deriving The Wind Speed Model

As shown by the example figure 11 from the 28th of May, although the peak of the Gaussian distribution falls at about  $x = 10.22$ , the linear pitch plot does not cross the x axis at the same value. This means that the Gaussian peak intersects the pitch plot at an angle given by  $y = \theta$ , corresponding to the INMS peak shift. This is illustrated in figure 12, where the arrow indicates the peak shift angle of the intersection between the INMS peak value and the pitch line. This suggests that the neutral winds are not necessarily horizontal, but they can have a vertical component. As a result, the maximum number of counts collected by the INMS occurs when the INMS faces against the direction of the wind at an angle  $\theta$  to the horizontal.

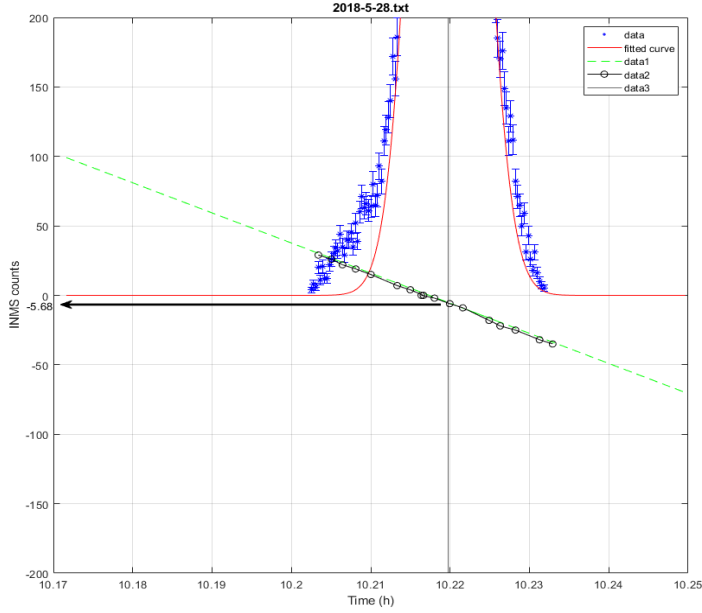


**Figure 12:** The Gaussian peak in figure 11 is zoomed in to calculate the INMS peak shift. For the 28th of May 2018, the shift of the high geometric factor occurs at  $-5.68^\circ$ , as demonstrated by the arrow.

In order to investigate these neutral winds, the flux associated with the neutral wind field is modelled as a cylinder of volume  $V$ . If the cylinder contains a total  $N$  number of particles, then the particle's number density  $N_e$  can be calculated as:

$$N_e = \frac{N}{V} \quad (4.1)$$

According to the divergence theorem [18], the particle flux across a surface  $S$  is equal to the volume enclosed by that surface. If the flux across a surface is represented by the neutral wind field  $w$ , the total flux through this volume per second is given by:

$$\int \vec{F} \cdot d\vec{S} = (\vec{w} \cdot \hat{r})S \quad (4.2)$$

where  $\hat{r}$  represents the unit vector pointing in the direction in which the INMS faces. Simplifying the right hand side of equation 4.2 results in the horizontal component of the flux:

$$(\vec{w} \cos \theta) S \quad (4.3)$$

The net flux entering the INMs is going to be represented by the relative horizontal velocity between the wind and the CubeSat, which is given by:

$$(\vec{w} \cos \theta) - \vec{v} \quad (4.4)$$

As the volume of the cylinder corresponds to the net flux, the  $V$  term in equation 4.1 can be substituted by equation 4.4. This results in the following formula:

$$N = N_e (\vec{w} \cos \theta - \vec{v}) S \quad (4.5)$$

The model is then finalised by the inclusion of a calibration factor  $f$ . This variable attempts to include real thermospheric changes that a simple model based solely on particle counts might not take into account. The calibration factor considers physical constants such as solar flux, solar activity and geomagnetic activity, which affect plasma drift and ion-neutral collisions. Hence, the final version of the model is:

$$Nf = N_e (\vec{w} \cos \theta - \vec{v}) S \quad (4.6)$$

In this project,  $N$  represents the INMS counts,  $N_e$  is the oxygen number density and  $\vec{w}$  is the neutral wind speed. The other constants are the velocity of Phoenix  $\vec{v}$ , which was measured to be  $7730 \text{ ms}^{-1}$  and the surface area  $S$  of the INMS which was calculated to be  $1.37 \times 10^{-6} \text{ m}^2$ . Once a calibration factor is calculated using the HWM model, a linear fit of equation 5.1, over the INMS counts plotted against IRI number densities, can be used to estimate a value for the neutral wind speeds.

#### 4.4.4 Graphs and Plots

To gain better understanding of the data set, the trajectory of the CubeSat was plotted. An example plot of the path that Phoenix orbited along, during which the INMS collected data, is shown by the blue dots in figure 13. As the CubeSat travelled from west to east, the first

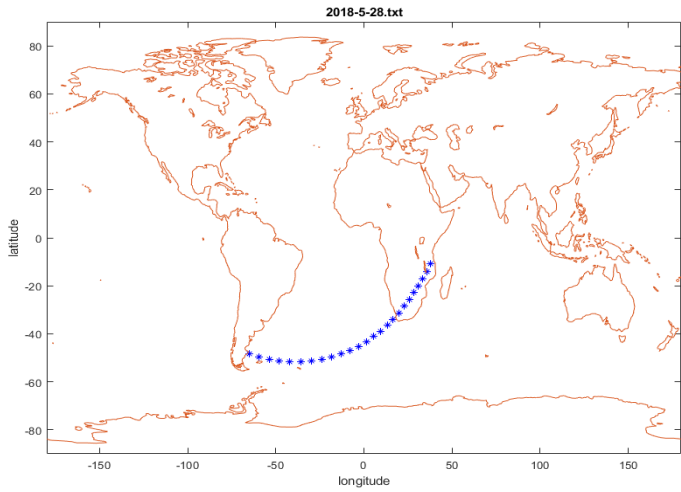


**Figure 13:** Trajectory of Phoenix as the INMS took readings of oxygen particles ( $O_+$ ) during the flight on the 28th of May 2018.

data point on the left indicates the location at which the INMS was first switched on, on the 28th of May 2018.

The HWM model, in conjunction with the trajectory in figure 13, was computed to illustrate the wind vector fields at Phoenix's average altitude for that corresponding day, as shown in figure 14. The appendix A.3 shows the MATLAB code of these vector fields. This kind of plot is particularly useful to investigate the relationship between the direction of the horizontal wind speeds and the INMS counts. Other useful plots were made using the NRLMSISE model and the IRI model, whose code is shown in appendix A.4. Example of such plots demonstrate the change in oxygen density along the path of the CubeSat. This is shown in figure 15, where the red data points indicate the NRLMSISE oxygen densities with respect to the time of flight of Phoenix. Hence, while IRI is used to calculate the number density of  $O_+$ , the impact of varying atomic oxygen density is investigated using the NLRMSISE. Numerical values from IRI are used in this project under the assumption that plasma drifts are equal to neutral winds, because at mid-low latitudes there is a reduction in ion drifts [3].

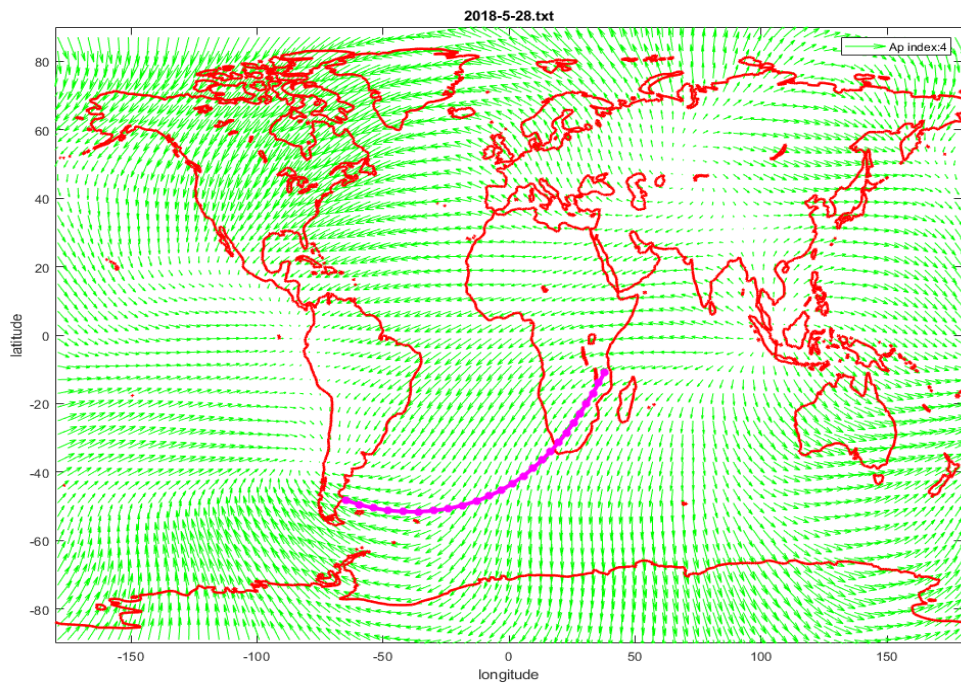


**Figure 14:** HWM wind vector field and the trajectory of Phoenix while the INMS collects data on the 28th of May 2018.

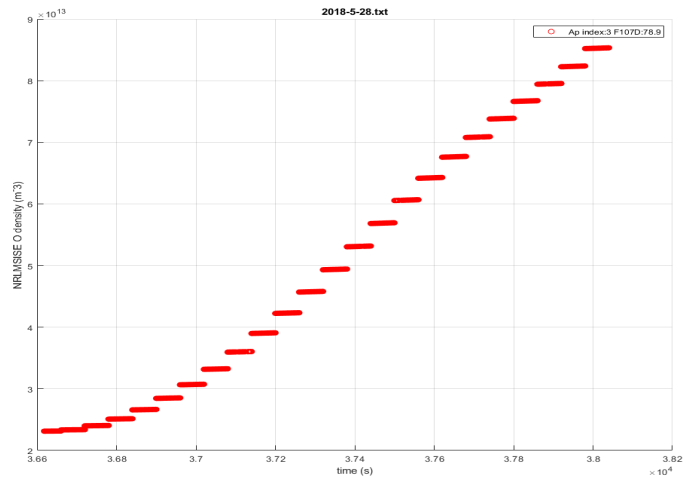


**Figure 15:** NRLMSISE Oxygen density plot along the flight of Phoenix on the 28th of May 2018.

## 5 Results and Analysis

### 5.1 Simultaneous Equations Method

The first method, which was adopted in order to calculate the neutral wind velocity  $w$  and the calibration factor  $f$ , involves the use of simultaneous equations. The HGF peaks, which are demonstrated under figure 16, were selected from both the 27th of May and 28th of May as they had an appropriate number of counts and a reasonable Gaussian distribution. The first step involved finding the INMS peak shift from both graphs 16a and 16b, as described in section 4.4.3 and illustrated in the example figure 12. After finding the respective oxygen number densities  $N_e$ , two simultaneous equations were set up using equation 4.5. The results are shown in table 1. The neutral wind speed was calculated to be  $8184.2\text{ms}^{-1}$ , which is totally incorrect as thermospheric neutral winds do not exceed over  $600\text{ms}^{-1}$  [3]. In order to determine an expected value for  $w$ , the HWM was used to find the expected wind velocity at the location and time of the two peaks, which gave an average horizontal wind speed of about  $120\text{ms}^{-1}$ .

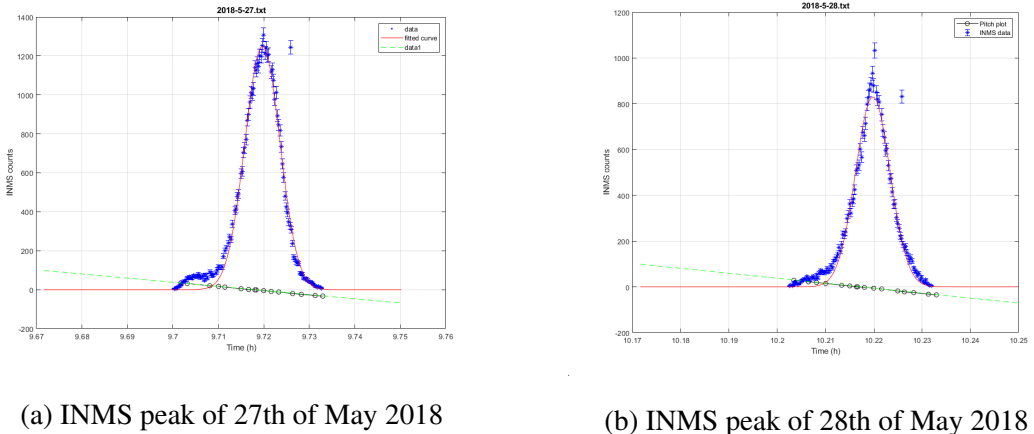


**Figure 16:** High geometric factor peaks from two consecutive days, plotted with their respective pitch line.

The calculated neutral wind speed exceeded the expected wind speed by 67 times. The accuracy of this approach relied on certain assumptions. Both the 27th of May and 28th of May, measured the same  $Ap$  value of 3 and F10.7cm values of 76.6 and 78.9 respectively.

In addition to the  $Ap$  and F10.7 indices, the trajectory of Phoenix during data collection, the time of the day and the O+ densities were all fairly similar across the two days. Therefore, it was reasonable to assume that the simultaneous equations approach would produce the same  $f$  and  $w$  values across these two dates.

$f$	$w$
$3.34 \times 10^4$	$8184.2 \text{ms}^{-1}$

**Table 1:** Results from the simultaneous equation method.

## 5.2 Clustering Data

In order to better understand the nature of the discrepancy between expected and the observed neutral wind speed, the INMS data were plotted against the IRI's number densities. The analysis was conducted to investigate the relationship between the INMS counts  $N$  and the number density  $N_e$ , which was expected to be linearly proportional. For a fair comparison, the chosen days had similar  $Ap$  and F10.7cm indices with quiet geomagnetic and solar conditions. Peak values from each Gaussian distribution were extracted from the full run INMS plots such as the one described in figure 9. The corresponding time and spatial coordinates were also used to obtain a value for the oxygen number density (O+). These were then plotted against each other via an excel spreadsheet to obtain the graphs in figure 17. Figure 17a, shows the distribution of the data with respect to their date, represented by the colour. Figure 17b represents the same plot but categorized for day-night distinction. The orange points illustrate the INMS data gathered while Phoenix was in the dayside of the Earth, whereas the green data points mark the INMS counts collected during the night. This was established by inspecting the trajectories shown in figure 13 together with an online terminator [19]. It demonstrated that most of the dayside counts were collected in May, while the night side data was gathered in June.

By inspecting 17b, it is seen that there is a clear clustering between the dayside and night side data points. Due to higher oxygen density during the day time, the day side data

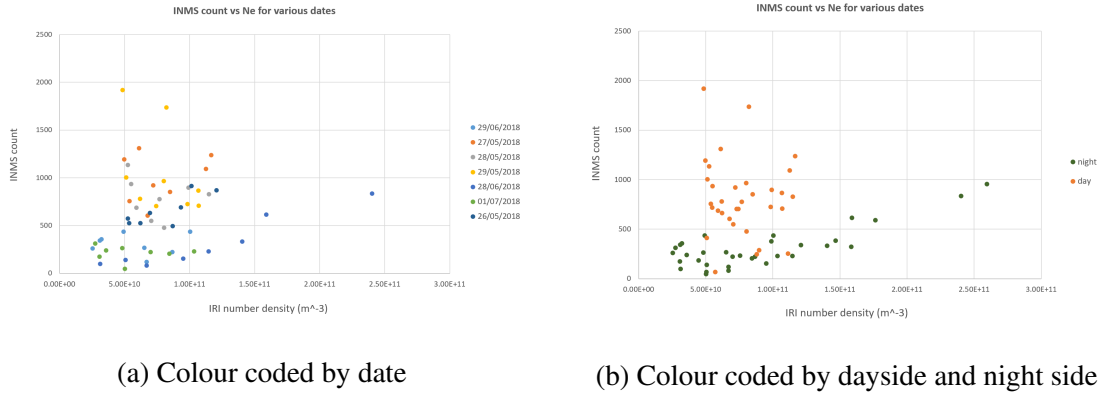


**Figure 17:** INMS counts against IRI Oxygen number density for 8 different dates.

points are expected to be in the higher right hand corner of the plot, while the night side data points are predicted to be in the lower left hand corner. Although there is an approximate linear correlation between  $N$  and  $N_e$  for the night side data, the distribution of day side points demonstrates unquantifiable randomness. In addition, it should be acknowledged that, in the day side, the density is not proportionally higher with respect to counts, which means that something else could be causing the number of counts to be higher than usual. In order to interpret this variability in the data, further analysis is done using empirical models.

### 5.3 Day and Night Subplots

#### 5.3.1 INMS counts Subplots

In order to further evaluate the INMS data, HGF from different days were compared through subplots. This is illustrated in figure 19, where each plot from the first row displays the HGF INMS counts collected while Pheonix was in the dayside of the Earth. Wheras the second row illustrates the HGF factor peaks from the night side data. The date for each plot is shown above. Upon inspection, the figure shows that the dayside HGF counts have higher and more prominent peaks compared to the nightside distributions. This is anticipated, as higher number of counts are expected due to larger atomic oxygen densities ( $O^+$ ) during the day. In addition, the difference in geo-location could also have a huge impact on the number of counts across different days. In fact, the day side counts correspond to the data collected by the CubeSat during a flight between South America and West Africa as shown in figure

[18a](#). While the night side data represents the counts collected near the south Pacific Ocean as shown in figure [18b](#). Although atmospheric variables may be vastly different between these two locations, seasonal variations can be ruled out as both trajectories happen to be in regions of the southern hemisphere. By investigating the dayside data, it is observed that 27th, 28th and 29th of May show much higher Gaussian peaks. Assuming that the data was collected during similar solar and geomagnetic conditions, it is unexpected to see hugely different sizes of peaks between consecutive days as the counts in this region are also collected approximately at the same universal time each day. This relatively high counts for these last 3 days could be explained by a sudden increase in atomic oxygen density O+, which may not be observed by IRI as this is a climatology model and hence small scale changes are not detected. Having minimised all other physical and spatial variations, neutral winds could also be responsible for the variation observed in the dayside distributions.

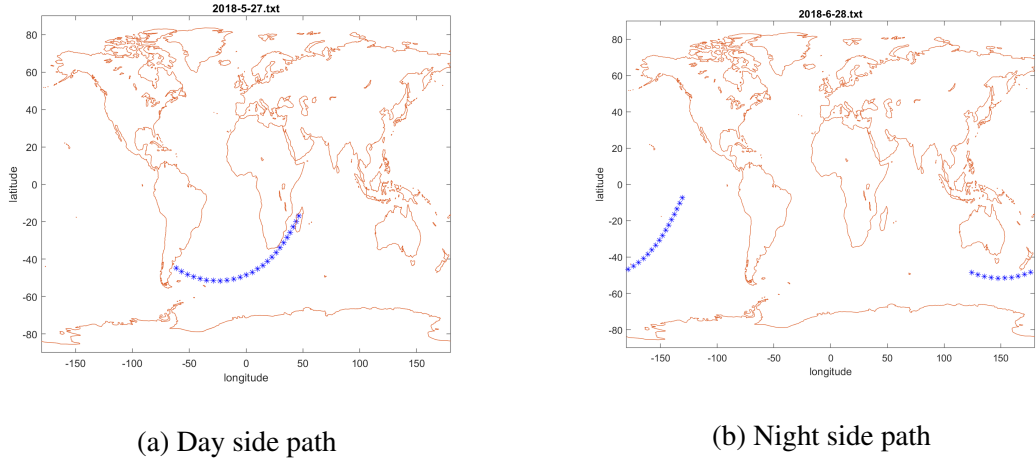


**Figure 18:** Path of Phoenix while the INMS collects data. Trajectory of dayside counts are all similar to figure [18a](#). Trajectory of night side counts are all similar to figure [18b](#)

### 5.3.2 HWM and NRLMSISE Subplots

To investigate a possible surge in oxygen densities, subplots of the NRLMSISE model for the corresponding dates are shown in figure [20](#), which illustrates the changes in neutral atomic oxygen density (O) along the path of the CubeSat. As expected, during the day, densities are observed to increase as the CubeSat travels from high latitudes to the equatorial zone.

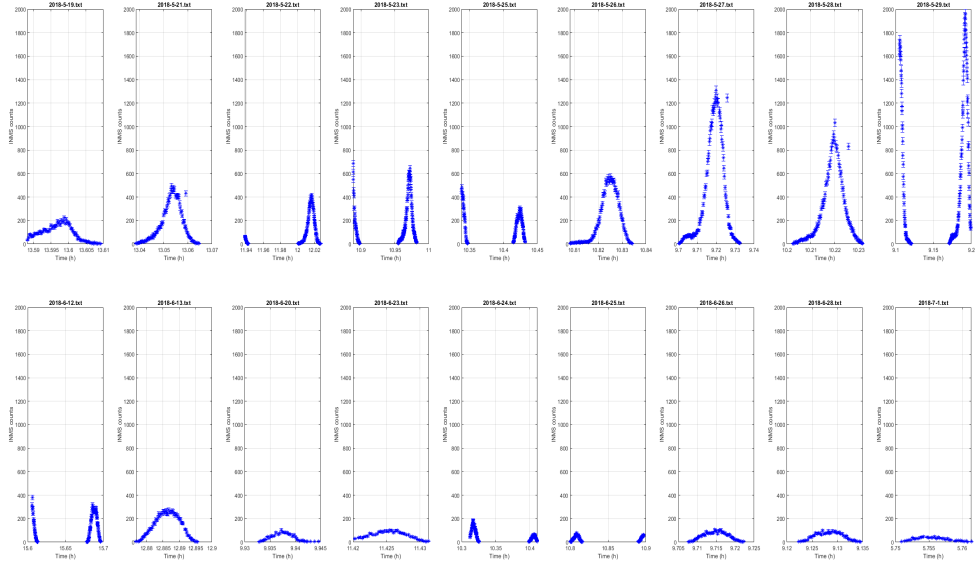


**Figure 19:** Subplot of high geometric factor peaks of selected dates with quiet conditions. First row of subplots indicate the dayside INMS counts, while the second row of subplots indicate the nightside INMS counts.

However the plots in the first row are largely uniform as they follow the same increasing pattern, which suggest that there should not be a sudden increase in the number of counts, as there is no drastic change in neutral densities. In contrast, the night side density plots show much more variability considering that the path of the CubeSat is approximately equal across the different days in the bottom row. This could be because night side days present variability in geomagnetic activity and solar flux, as shown by the  $A_p$  and  $F_{10.7}$  indices in figure 19. As the time at which the INMS is turned on each day is not exactly the same, this could also be a factor for the differences in densities.

The HWM model shown in figure 21 illustrates the velocity of neutral particles along the path taken by Phoenix during which the INMS counts were collected. Appendix A.5 shows the MATLAB scripts for these graphs. As described previously, the subplots correspond to the same days represented by the plots in figure 19 and 20. The figure compares the changes in the magnitude of the wind speeds between different days. While the magnitudes of the wind speeds shown in the first row follow approximately the same pattern across

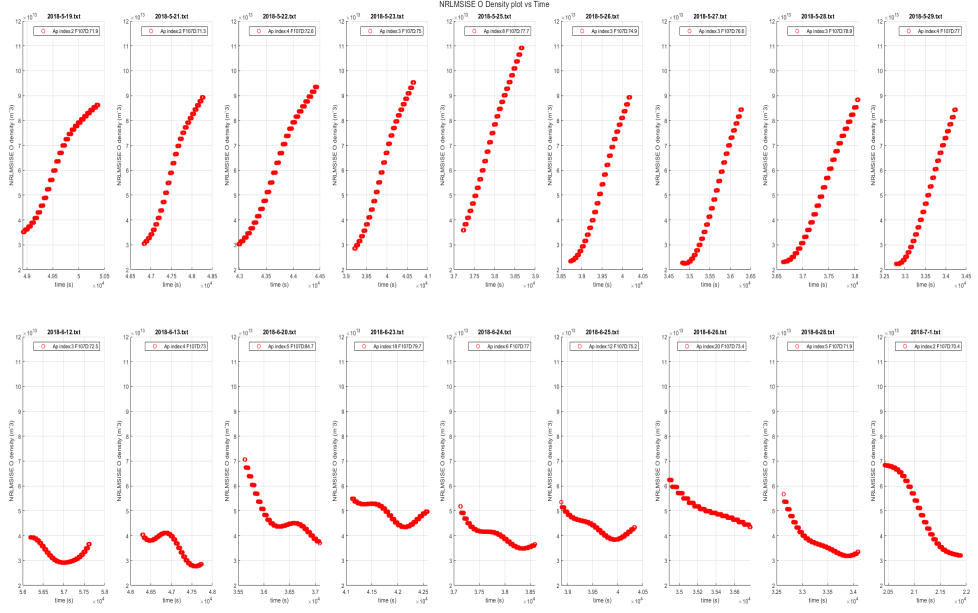


**Figure 20:** Subplots of the NRLMSISE model of oxygen density O along the trajectory of the CubeSat while the INMS is on. First row of subplots indicate the dayside density, while the second row of subplots indicate the nightside density.

different days, the night side wind speeds are affected by much more volatility as they vary from lows of  $10\text{ms}^{-1}$  to highs of  $180\text{ms}^{-1}$ . This demonstrates that in addition to the variability in density seen in figure 20, the fluctuations in wind speeds could also have an impact on the counts collected by the INMS. However, to understand to what extent the neutral wind speeds have affected the INMS data, it is necessary to investigate the dependency of the INMS counts on the direction of the wind vectors.

#### 5.4 HWM Vector Fields

Maps of the HWM vector field overlaid on NRLMSISE density contours were created for each day using MATLAB as shown in appendix A.6. The path of Phoenix is also traced, demonstrating how the wind fields and oxygen densities ( $\text{O}^+$ ) change with respect to the CubeSat's flight. An example map of the 19th of May is shown in figure 22, where the green arrows indicate the HWM wind vectors. As the CubeSat rotates about its ram axis, more counts should be recorded by the INMS if thermospheric winds push particles into the

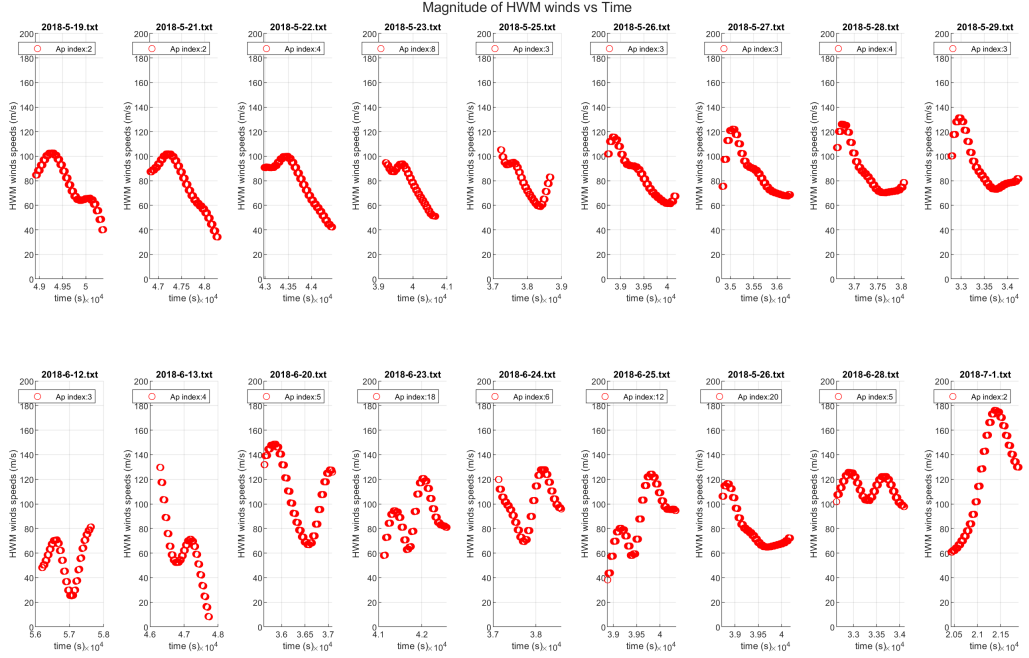


**Figure 21:** Subplots of the wind speeds calculated by the HWM model along the trajectory of the CubeSat while the INMS is on. First row of subplots indicate the dayside wind speeds, while the second row of subplots indicate the nightside wind speeds.

INMS's apertures. Inspecting figure 22, the horizontal wind vectors are broadly observed to travel diagonally across the magenta path, implying that the winds do not flow against the INMS look direction, but rather they are incident on one of the sides of Phoenix. As a result, the number of INMS counts collected are fewer, leading to a smaller HGF peak. In contrast, if the wind vector field of the 27th of May is examined, the opposite is true. As shown in figure 23, the cyan circle indicates the part of the CubeSat's path that collects the HGF data. The wind vectors in that section of the path, point in a direction that is anti-parallel to the direction of motion of the CubeSat. As long as the horizontal winds are directed within the field of view of the spacecraft, the winds flow towards the CubeSat pushing particles into the INMS's apertures. This results in a high number of counts, which could explain the large HGF peak observed for the 27th of May relative to the Gaussian peak from the 19th of May, as seen in figure 19. To confirm this observation, the wind field maps of the 29th of May and 20th of June are illustrated in figure 24. Like before, the cyan circle indicates the

position at which the HGF counts are collected. Inspecting figure 24a, the number of counts are expected to be high as the wind vectors flow anti-parallel to the direction of Phoenix and hence push more oxygen particles into the INMS. In figure 24b, ignoring the horizontal magenta line connecting the cubeSat’s coordinates to the other side of the world, tail winds are observed, which could be responsible for the low INMS counts. These observations are again confirmed in figure 19, by the size of their respective peaks. Further investigation proved that the dates that demonstrated a general head on wind pattern are the 26th, 27th, 28th, 29th of May.

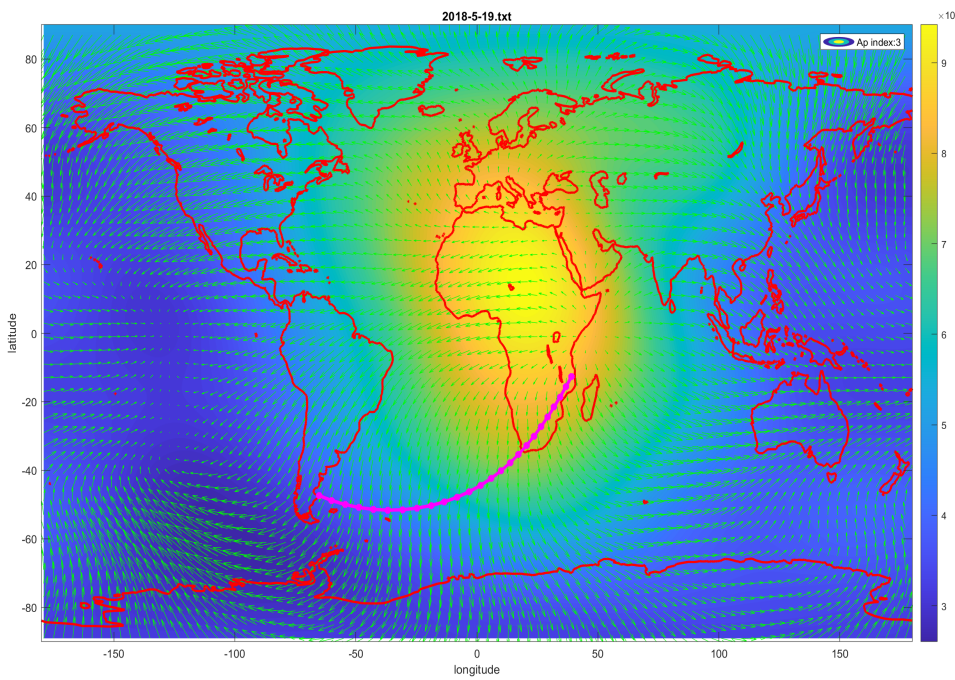


**Figure 22:** HWM vector wind field overlaid on top of the NRLMSISE density contours for the 19th of May. The magenta path indicates the trajectory traced by Phoenix while the INMS was turned on.

One important aspect to consider into these observations is the field of view of the instrument. As the horizontal field of view of the CubeSat is  $\pm 2^\circ$ , no atomic oxygen ( $O_+$ ) particles are expected to enter the CubeSat unless the horizontal wind vector flows into the INMS within the allowed field of view. In order to verify this, calculations were performed

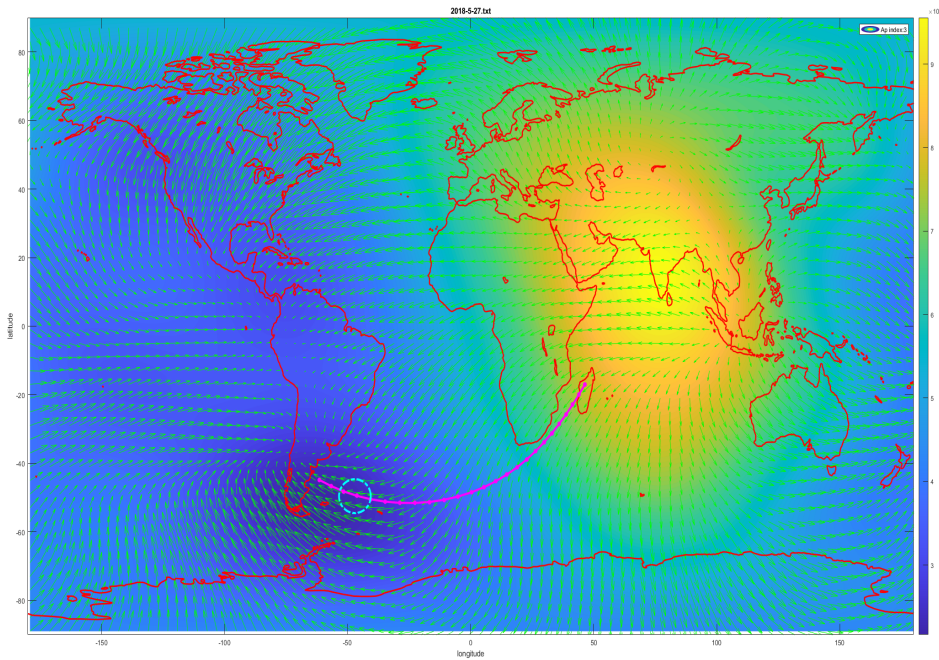


**Figure 23:** HWM vector wind field overlaid on top of the NRLMSISE density contours for the 27th of May. The magenta path indicates the trajectory traced by Phoenix while the INMS was turned on.

using the HWM model and the coordinates of the CubeSat’s trajectory to find the difference in angle between the INMS’s velocity direction and the HWM wind vector. By finding an approximate value for the gradient of the trajectory at the HGF peak, the INMS’s velocity direction can be assumed from the inverse tan of the result. The value from this angle is then compared with the direction of the HWM model’s wind vector at the peak’s location. If the difference between the two angles is found to be smaller than  $+/-2^\circ$ , it is reasonable to conclude that the largest peaks arise purely because of thermospheric neutral winds being directly incident on the INMS. Appendix A.7 shows the details of these calculations. The results of the difference between these angles are shown in table 2, where each day corresponds to the four largest HGF peaks. No angles were found to be within the  $+/-2^\circ$  field of view. What is more interesting is that, although the 29th of May was observed to have the largest peak from figure 19, the direction of the wind with respect to the INMS’s aperture

was actually found to be  $-17.1^\circ$ , which is surprisingly greater than the angle calculated for the 27th or the 28th of May. This may suggest that there could be another justification for the varying sizes of the HGF Gaussian peaks observed in figure 19. However, as oxygen densities and wind vector magnitudes at the peaks were observed to stay broadly constant, one plausible explanation could be the fact that, in practice, winds may not follow strict straight line paths as indicated by the vector fields, but rather complex perturbations, caused by winds interacting with the CubeSat, making particles randomly enter the INMS even when the winds only partially flow towards the apertures. In addition, thermospheric winds can blow particles which could accumulate them in front of the CubeSat so that they may enter the INMS, despite the lack of a direct head on wind vector. It is crucial to mention that the angles calculated in table 2 are not the vertical peak shift angles  $\theta$  mentioned in section 4.4.3, instead they are angles in the horizontal  $xy$  plane which only compare the horizontal wind vectors to the INMS's velocity vector.

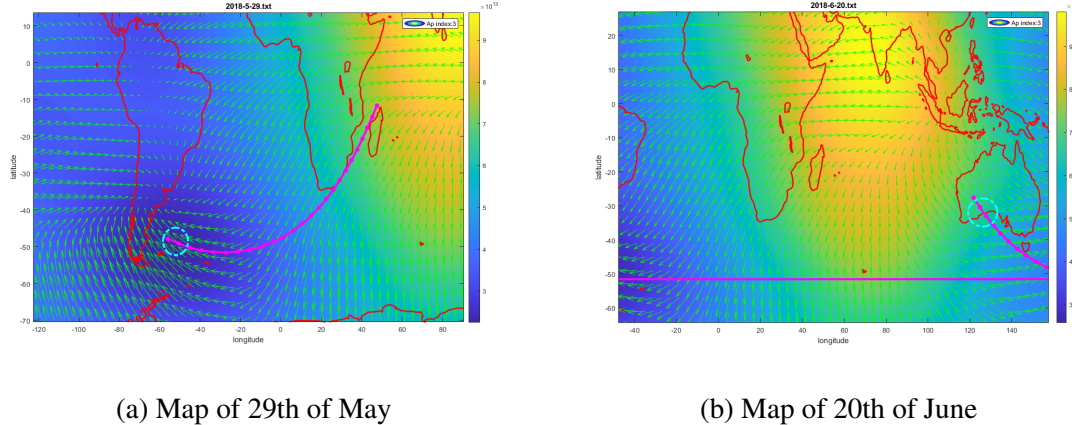


**Figure 24:** Comparing vector fields direction with Phoenix look direction.

2018 – 5 – 26	2018 – 5 – 27	2018 – 5 – 28	2018 – 5 – 29
$30.9^\circ$	$3.6^\circ$	$5.2^\circ$	$-17.1^\circ$

**Table 2:** Angle between the velocity vector and the HWM wind vector at the location of the HGF peak for four different dates.

## 5.5 Comparing Vector Fields and Full Run INMS Counts

An additional approach was also attempted where the full run of INMS counts for each day were compared to the corresponding wind field. An example is shown in figure 25, which compares the direction of the wind vectors to the INMS counts collected on the 26th of May. As the green arrows in figure 25a become more and more parallel to the trajectory, the maximum number of counts from each peak in 25b increases from about 600 to 950 counts. This is illustrated by the head on wind vectors near the South African region, which may correspond to the highest peaks observed around 900 counts. Although this clearly shows the correlation between INMS counts and horizontal wind speeds, most other dates do not seem to display this relationship.

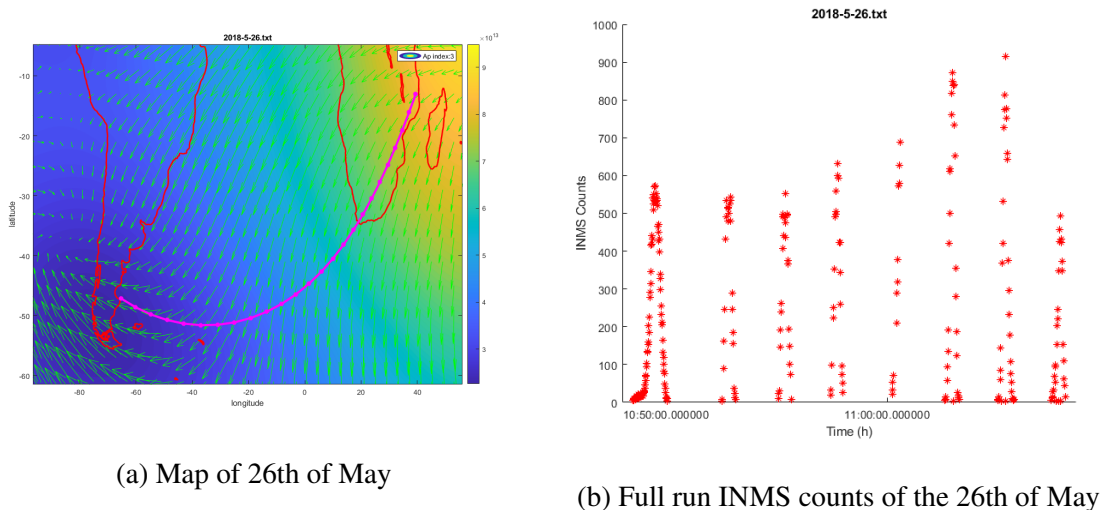


**Figure 25:** Comparing vector fields with the full run INMS counts for the 26th of May.

## 5.6 IRI O+ Density Model

Further investigating the role of O<sup>+</sup> densities, the NRLMSISE subplots shown in figure 20 were compared with IRI plots mapped by Ali Ozkidir [16], which were re-arranged in this project to match the dates in the NRLMSISE subplots, as demonstrated in figure 26. As anticipated, the plots for each day seem to show similar patterns. Despite IRI showing proportionally lower oxygen densities at night, it is not a surprising effect as this may happen because of electronic recombination.

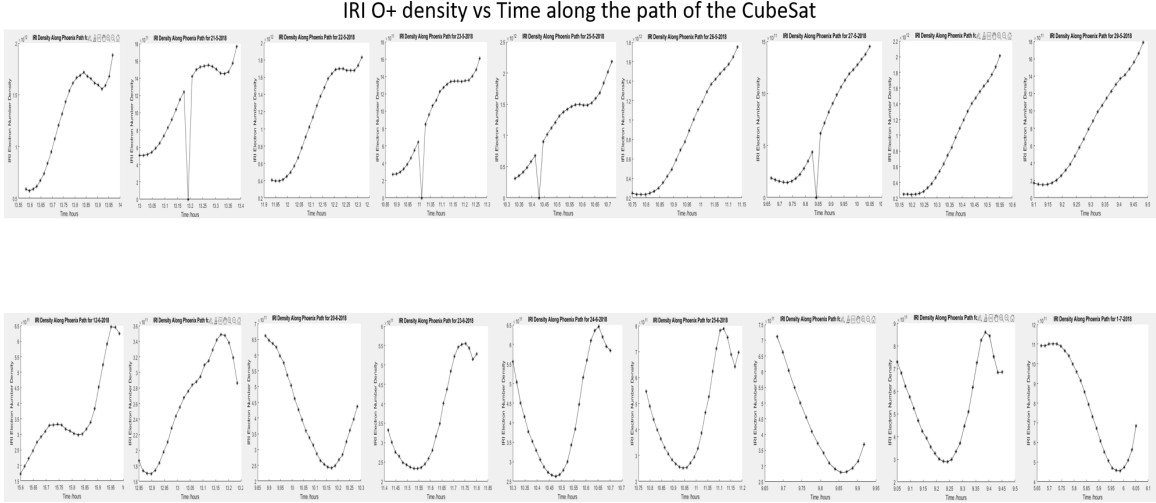


**Figure 26:** Subplots of the IRI model of oxygen density O+ along the trajectory of the CubeSat while the INMS was turned on. First row of subplots indicate the dayside densities, while the second row of subplots indicate the nightside densities.

An approach that was adopted in this project involved utilizing the maximum number of counts and oxygen number densities extracted and visualised in figure 17. The INMS counts and the O+ densities from IRI were then plotted on a single graph, as shown by the subplots in figure 27, where top and bottom row represent the day side and night side data, respectively. In order to maximise the comparability of the plots, the density values were scaled by a chosen numerical factor of  $10^{-8}$ . The 26th of May, 27th of May, 24th of June and 28th of June are dates for which the INMS counts roughly observe a similar pattern displayed by the density lines. Although this is evidence that the number of counts respond well to changes in O+ densities, the insufficient number of data points makes it difficult to draw conclusive interpretations. However, one interesting aspect of figure 27 is that the lines in the last three day side plots follow a very close pattern except for the first couple of points in each plot, where the INMS counts seem to be relatively high compared to the respective O+ densities. In addition, the night side counts tend to be considerably lower than the respective O+ densities, which could be explained by the absence of head on winds. Due to time constraints it was not possible to investigate plots from further dates.

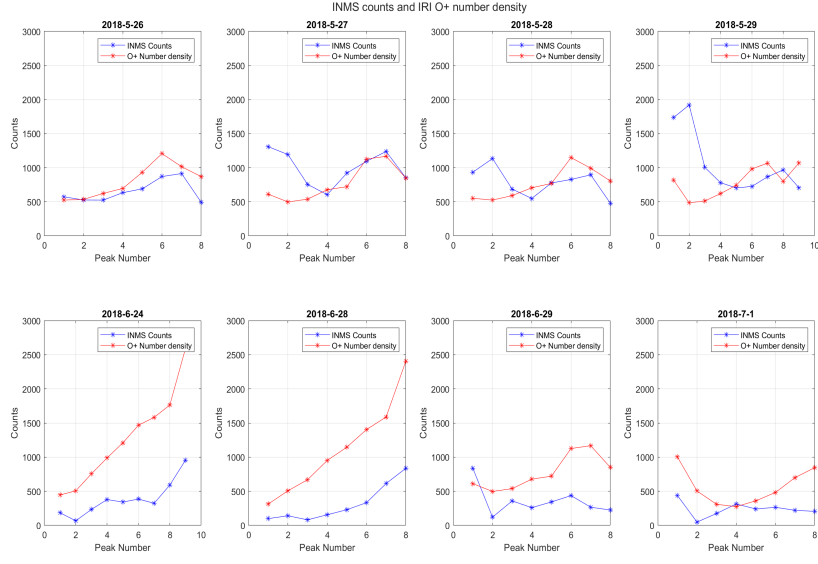


**Figure 27:** Subplots of maximum INMS counts and IRI O+ number densities plotted in the same graph. Eight different dates were chosen, as displayed above each plot. Top four dates are in the dayside and bottom four dates in the nightside.

### 5.7 Calculating the Calibration Factor and The Wind Velocity

The final step in this project involves analysing the data described in section 5.2 and visualised in figure 17. The same 8 days worth of data were imported into a MATLAB script and plotted as shown in figure 28. In order to fit a linear function to the data, equation 5.1 was rearranged in the following way:

$$N = \frac{(\vec{w} \cos \theta - \vec{v})S}{f} N_e \quad (5.1)$$

where the gradient is equal to  $\frac{(\vec{w} \cos \theta - \vec{v})S}{f}$ . This was calculated by first obtaining a value for the calibration factor  $f$ . As  $\vec{w} \cos \theta$  is equal to the winds entering the INMS horizontally, the green arrow in diagram 29 corresponds to the HWM wind speed.

By finding the average wind speeds at the location of the HGF peak for the 26th, 27th, 28th, 29th of May and by finding the average INMS counts for those days, as well as the corresponding average O+ number densities, equation 4.5 was used to compute a value for  $f$ , which is illustrated in table 3. Once the value of  $\theta$  is calculated from the average of the peak

shifts, equation 5.1 is applied in order to obtain the neutral wind speed from the gradient of the red linear function in figure 28. By rearranging the gradient, the results were obtained and shown in table 3. Although the neutral wind speed  $w$  is again totally miscalculated, the calibration factor  $f$  demonstrates an interesting feature. Using its value of  $9.59 \times 10^5$ , the value for the gradient  $\frac{(\vec{w} \cos \theta - \vec{v})S}{f}$  was manually calculated to be  $1.36 \times 10^{-8}$ , which is  $\approx 1 \times 10^{-8}$ . This now provides a reasonable justification for the use of  $10^{-8}$  for the scaling factor in section 5.6, confirming that the calibration factor  $f$  illustrated in table 3 maybe an acceptable value. Appendix A.8 shows the details of the calculation.

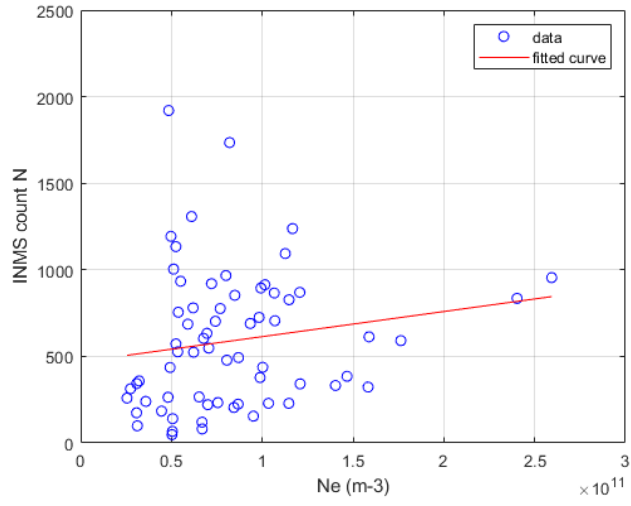


**Figure 28:** Linear fit of INMS counts against IRI oxygen number density ( $O+$ ) for 8 different dates. The red line indicates the gradient described in section 5.7.

$f$	$w$
$9.59 \times 10^5$	$6732.2 \text{ ms}^{-1}$

**Table 3:** Results from the gradient method

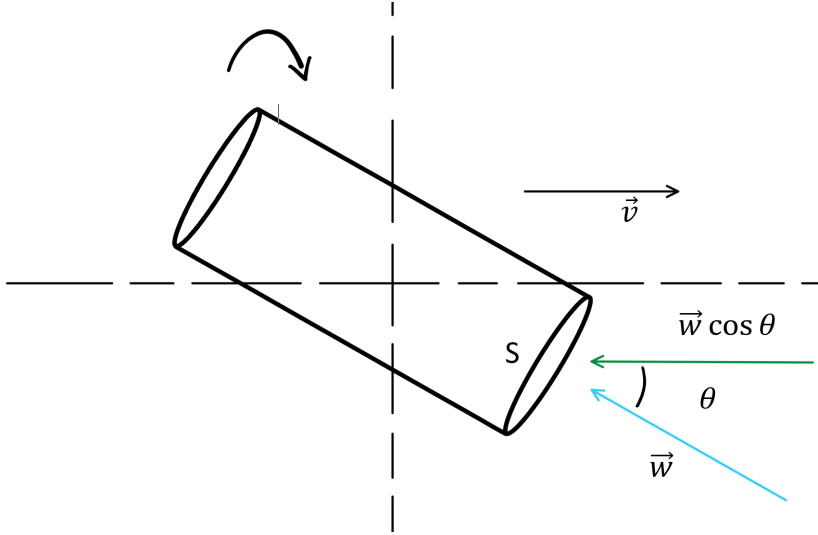


**Figure 29:** Two dimensional schematic diagram to illustrate the direction of all the vectors with respect to the INMS. The vertical axis is the  $z$  axis, whereas the horizontal axis shows the  $xy$  plane.

## 5.8 Discussion

One concluding, yet important observation to make, involves the usefulness of the Gaussian peak shift angle  $\theta$ . Despite describing the direction of the neutral winds, the value for the peak shift does not prove to be of any relevance in the calculations of magnitudes. A distribution of peak shift angles in appendix A.9 shows that  $\theta$  ranges from  $0^\circ$  to  $-8^\circ$ . Although the vertical field of view is  $+/-15^\circ$ , the peak shift angle is so small that  $\cos\theta$  itself does not alter the results, because  $\vec{w}\cos\theta$  can be approximated as  $\sim \vec{w}$ . Therefore, this confirms that the calculation of wind speeds are not as dependent on  $\theta$  as initially thought, but rather it is heavily influenced by the INMS counts, oxygen number densities and Phoenix's orbital speed. In addition, the  $+/-2^\circ$ horizontal field of view is also incredibly narrow that any relevant wind calculations can only be performed if the wind vectors directly flow head on against the INMS. As the velocity of Phoenix is more than 70 times larger than the neutral wind speeds, it becomes difficult to quantify a value for  $\vec{w}$  since any extra velocity that the particles gain from the wind is seen as marginal from Phoenix's reference frame. Moreover, effects of spacecraft charging can cause particle acceleration leading to discrepancies in wind calculations [22]. Physical effects such as these can be taken into account if the

counts were collected in the same location during both day and night, which would also further improve the data analysis. Lastly, further research is necessary to verify the value for  $f$  as thermospheric neutral winds are dependent on external physical factors that constantly affect the thermosphere.

## 6 Conclusion

The purpose of this project was to present an alternative method to investigate the ionospheric plasma drifts and the thermospheric neutral winds through a brand-new in-situ technique implemented via the Ion Neutral Mass Spectrometer (INMS) aboard of the Phoenix CubeSat. In order to achieve this, firstly, the method used in this project involved the analysis and visualization of the raw INMS data with respect to its peak shift angle, with the goal of confirming the observations drawn by previous research. Secondly, a derived linear relationship between INMS counts and oxygen number densities was adopted before the data was visually inspected with empirical models such as the HWM, NRLMSISE and IRI. The HWM vector field maps were able to explain reasonably well the varying sizes of the HGF INMS peaks observed in figure 19, where the large INMS counts corresponded to the wind vectors pointing head on towards the INMS. In order to estimate these winds, the derived model shown in equation 4.5 was used to linearly fit a scatter plot of INMS counts against IRI oxygen number densities ( $O+$ ). The resulting calibration factor  $f$  and neutral wind speed  $w$  were estimated to be  $9.59 \times 10^5$  and  $6732.2 ms^{-1}$ , respectively. Although this approach was theoretically appropriate, the discrepancy between estimated and observed wind velocity could be attributed to the actual practicality of the method. As the use of the peak shift angle resulted to be ineffective, the method only fully relies on INMS counts and corresponding number densities from empirical models. Hence, in order to improve the estimates, the INMS should be programmed to collect data for longer than 20-25 minutes each day, which could be done if the INMS is turned on in the same location for a period of time during both day and night, as a more comprehensive comparison can be performed. It is also important to mention that, despite these INMS textfiles were thought to have been originally created by Ali Ozkidir, it was later found out that the authorship is actually unknown. However,

the data sets were verified against the raw INMS counts extracted by PhD student Sachin Reddy, even though the location data is not yet replicable. Future research, should also try to implement a relevant attitude control system, which may reduce the pitching and tumbling of the CubeSat, allowing for a constant inflow of particles into the INMS. This could also be further improved by increasing the field of view of the apertures for better particle detection.

## Acknowledgments

I would like to thank my supervisor Dr. Anasuya Aruliah for the huge support offered during the project, by providing me with feedback, information and time management tips. I would also like to thank Prof. Dhiren Kataria for providing me with technical assistance. Finally, I would like to massively thank PhD student Sachin Reddy, who granted support through resources and organised meetings.

## References

- [1] Picone, J. M. et al., 2002. *NRLMSISE-00 empirical model of the atmosphere: Statistical comparisons and scientific issues*. Journal of Geophysical Research: Space Physics, 107(A12), pp.SIA 15–1-SIA 15–16.
- [2] Kutiev, Ivan et al., 2013. *Solar activity impact on the Earth's upper atmosphere*. Journal of space weather and space climate, 3, p.A06.
- [3] Solomon, S.C & Roble, R.G, 2015. Thermosphere. In *Encyclopedia of Atmospheric Sciences*. Elsevier Ltd, pp. 402–408.
- [4] Rees, M.H., 1989. *Physics and chemistry of the upper atmosphere / M. H. Rees*, Cambridge University Press.
- [5] Mohanakumar, K., 2008. *Stratosphere troposphere interactions : an introduction / K. Mohanakumar.*, Dordrecht: Springer.
- [6] Laštovička, Jan, 2006. *Forcing of the ionosphere by waves from below*. Journal of atmospheric and solar-terrestrial physics, 68(3), pp.479–497.

- [7] Emmert, J. T, Lean, J. L & Picone, J. M, 2010. *Record-low thermospheric density during the 2008 solar minimum*. Geophysical research letters, 37(12), p.n/a.
- [8] Kutiev, Ivan et al., 2013. *Solar activity impact on the Earth's upper atmosphere*. Journal of space weather and space climate, 3, p.A06.
- [9] Xu, Heqiucen et al., 2019. *Thermospheric wind variations observed by a Fabry–Perot interferometer at Tromsø, Norway, at substorm onsets*. Earth, planets, and space, 71(1), pp.1–13.
- [10] Aruliah, Anasuya et al., 2019. *Comparing high-latitude thermospheric winds from Fabry-Perot interferometer (FPI) and challenging mini-satellite payload (CHAMP) accelerometer measurements*. Annales geophysicae (1988), 37(6), pp.1095–1120.
- [11] Drob, Douglas P et al., 2015. *An update to the Horizontal Wind Model (HWM): The quiet time thermosphere*. Earth and space science (Hoboken, N.J.), 2(7), pp.301–319.
- [12] Sezen, Umut, Gulyaeva, T.L Arikán, Feza, 2018. *Online computation of International Reference Ionosphere Extended to Plasmasphere (IRI-Plas) model for space weather*. Geodesy and Geodynamics, 9(5), pp.347–357.
- [13] Minna, Palmroth, et al., 2020. *Lower thermosphere – ionosphere (LTI) quantities: Current status of measuring techniques and models*. Ann. Geophys. Discuss., <https://doi.org/10.5194/angeo-2020-42>, in review.
- [14] Vila, Fernández M., 2010. *Mission analysis of QB50, a nanosatellite intended to study the lower thermosphere*.
- [15] Reusch, William, 2020. *Mass Spectrometry*., Chemistry Libretexts, viewed 12 March 2021, [https://chem.libretexts.org/Bookshelves/Organic\\_Chemistry/Supplemental\\_Modules\\_\(Organic\\_Chemistry\)/Spectroscopy/Mass\\_Spectrometry](https://chem.libretexts.org/Bookshelves/Organic_Chemistry/Supplemental_Modules_(Organic_Chemistry)/Spectroscopy/Mass_Spectrometry).
- [16] UCL, MSSL. *Private Communication*.
- [17] Ali, Ozkidir, 2019 - *Investigating Ionospheric Density Using O+ Data From CubeSat INMS*. University College London, Department of Physics and Astronomy, MSc project.
- [18] Šilhavy, Miroslav, 1985. *The existence of the flux vector and the divergence theorem for general Cauchy fluxes*. Archive for rational mechanics and analysis, 90(3), pp.195–212.
- [19] Timeanddate, *Day and Night World Map*., timeanddate.com, viewed 29 February 2021,

<https://www.timeanddate.com/worldclock/sunearth.html?day=27&month=5&year=2018&hour=9&min=40&sec=0&n=&ntxt=&earth=0>.

- [20] McCloskey McCloskey, J. A., 1990. *Mass spectrometry / edited by James A. McCloskey.*, San Diego: Academic Press.
- [21] Dhiren Kataria. *Private Communication.*
- [22] Garrett, H.B, *The charging of spacecraft surfaces.* Reviews of Geophysics and Space Physics, vol. 19, no. 4, pp. 577-616, Nov. 1981.
- [23] Perry, A. H, 1984. Gill, A.E. *Atmosphere-ocean dynamics.* (Book Review). Progress in Physical Geography, 8(2), p.291.

# A Appendix

## A.1 Python Data Cleaning Script

This a Python code written in Jupyter Notebook. The routine removes all the systematic errors observed in the original textfiles, as described in section 4.4.1.

In this next cell, the code iterates over all the INMS text files contained in the directory. This will be read into a pandas dataframe, with which erranous lines are going to be removed. The dataframe is then going to be saved as a text file into a new directory.

```
In [ ]: 1 import os
2
3 ### changes working directory to
4 os.chdir(r"C:\Users\rifat\OneDrive - University College London\Rifat's PC\UCL\Y4\Project\MATLAB\Ali's MATLAB Work-20191010T1"
5 directory = r"C:\Users\rifat\OneDrive - University College London\Rifat's PC\UCL\Y4\Project\MATLAB\Ali's MATLAB Work-2019101
6
7 ### Loops over all the files in the directory
8 for filename in os.listdir(directory):
9     if filename.endswith(".txt"):
10         data = pd.read_csv(filename, sep = ' ', header = None, error_bad_lines = False)
11         ### new directory to save new corrected files
12         directory = r"C:\Users\rifat\OneDrive - University College London\Rifat's PC\UCL\Y4\Project\MATLAB\CorrectINMSdata"
13         print(os.path.join(directory,filename))
14         data.to_csv(os.path.join(directory,filename), header=None, index=None, sep=' ', mode='a')
15     else:
16         continue
17
18
```

## A.2 MATLAB Code for Plotting Gaussian To Full Run INMS Counts

This MATLAB function imported the INMS textfiles and extracted the counts and time column. The function plotted the INMS counts against time.

```
function [gauss_plot, inms_plot, Dt, inms, new_inms, f] = inms_import(textfile)
    % function imports the INMS textfiles and extracts the time columns and
    % the INMS counts columns. Plots Gaussian distributions on scatter
    % plots of INMS counts vs Time (h).

    % For this function to work it is necessary to
    % save this function into the same directory/folder as the INMS
    % textfiles.

    % importing INMS and time columns from textfiles
    d = importdata(textfile, ' ');
    Dt = duration(d.textdata(:,2),'InputFormat','hh:mm:ss.SSSSSS','Format','hh:mm:ss.SSSSSS');
    inms = d.data(:,4);

    %%new array to remove zero count clutters
    new_inms = zeros(length(inms),1);
    for i = [1:length(inms)]
        if inms(i) > 3
            new_inms(i,1) = inms(i);

        else
            new_inms(i,1) = nan;
        end
    end

    % creating scatter plot of INMS vs Time
    figure
    inms_plot = scatter(Dt,new_inms,'r*')
    xlabel("Time (h)")
    ylabel("INMS Counts")
    title(textfile)

    % plotting Gaussian fits to scatter plot
    figure
    f = fit(hours(Dt),inms,'gauss8','Exclude', inms < 50,'Robust','LAR')
    gauss_plot = plot(f,hours(Dt),new_inms)
    xlabel("Time (h)")
    ylabel("INMS Counts")
    title(textfile)
|
end
```

### A.3 MATLAB Code for The HWM Vector Fields

This is a MATLAB function that reads the INMS textfiles and, given an Ap index, computes the HWM wind vector fields for a given day. A trace of Phoenix's path is also illustrated.

```

function [vector_field] = HWM_vectorfield(textfile,ap)
% Computed the HWM vector field using the all the parameters from the
% textfiles and given an Ap index value for that day. The trajectory o
% of Phoenix is also traced.

% For this function to work it is necessary to
% save this function into the same directory/folder as the INMS
% textfiles.

%%% wind vector fields
%cd ("C:\Users\user\OneDrive - University College London\Rifat's PC\UCL\Y4\Project\MATLAB\CorrectINMSdata"); %path
disp("Plotting HWM wind vector field for each day")

date = importdata(textfile,' ');
lon = date.data(:,1);
lat = date.data(:,2);
h = mean(date.data(:,3)*1000);
days = day(datetime(date.textdata(1,1)), 'dayofyear');
time = seconds(duration(date.textdata(600,2),'InputFormat','hh:mm:ss.SSSSSS','Format','hh:mm:ss.SSSSSS'));
api = ap;

%lat5 = [1:3:180];
%lon5 = [1:3:360];
lat5 = [1:4:180];
lon5 = [1:4:360];
w_mat5 = nan(180,360);
w_mat6 = nan(180,360);
for i = lat5
    for j = lon5

        wind_vel5 = atmoshwm(i-91,j-181,h,'day',days,'seconds',time,'apindex',api,'model','total','version','14');
        w_mat5(i,j) = wind_vel5(1); %meridional wind matrix
        w_mat6(i,j) = wind_vel5(2); %zonal wind matrix

    end
end

%%% plot

load coastlines.mat;
[X,Y]= meshgrid(-179:180, -89:90);
vector_field = quiver(X,Y,w_mat6,w_mat5,10,"g","LineWidth",0.5)
hold on;
plot(coastlon, coastlat,"r","LineWidth",2)
box on
hold on
plot(lon, lat, "m*-", "LineWidth",3)
xlim([-180 180])
ylim([-90 90])
xlabel("longitude")
ylabel("latitude")
hold off
title(textfile)
legend(strcat("Ap index:",num2str(ap)))

```

## A.4 MATLAB Code for NRLMSISE Oxygen Densities Along Phoenix Path

This is a MATLAB function that reads the INMS textfiles and, given Ap and f10.7 indices, computes the NRLMSISE oxygen densities (O) against time plot for a given day.

```
function [density_vs_time, Ox] = nrlmsise_alongpath_time(textfile, f107A, f107D, ap)
% Plotting nrlmsise00 oxygen densities along Cubesat trajecotry
% for each day against time. Takes all parameters from textfiles as well
% as F10.7 monthly average, F10.7 daily average and Ap index

% For this function to work it is necessary to
% save this function into the same directory/folder as the INMS
% textfiles.

%%% NRLMSISE Oxygen densities along the trajectory of the Cubesat

cd ("C:\Users\Rifat\OneDrive - University College London\Rifat's PC\UCL\Y4\Project\MATLAB\CorrectINMSdata"); %path
disp("Plotting nrlmsise densities vs time for a chosen day along CubeSat directory")

date = importdata(textfile,' ');
lon = date.data(:,1);
lat = date.data(:,2);
h = date.data(:,3)*1000;
days = day(datetime(date.textdata(:,1)), 'dayofyear');
time = seconds(duration(date.textdata(:,2),'InputFormat','hh:mm:ss.SSSSSS','Format','hh:mm:ss.SSSSSS'));
api = repmat(ap,length(h),1);
[T, rho] = atmosnrlmsise00(h, lat, lon, 2018, days, time, f107A, f107D, api); % computing NRLMSISE model
Ox = rho(:,2); % extracting oxygen density

% plotting routine
density_vs_time = scatter(time,Ox,"ro")
ylabel("NRLMSISE O density (m^-3)");
xlabel("time (s)");
grid on;
title(textfile);
legend(strcat("Ap index:",num2str(ap)," F107D:",num2str(f107D)));
end
```

## A.5 MATLAB Code for HWM Wind Speed Along Phoenix Path

This is a MATLAB function that reads the INMS textfiles and given an Ap index computes the HWM wind speeds against time plot for a given day, along the path of Phoenix.

```
function [wind_vs_time] = hwm_alongpath_time(textfile,ap)
% function plots the winds computed by the HWM model along the
% CubeSat trajectory for each day against time. Takes in all the
% parameters from the textfiles and an Ap value for that day. Outputs a
% graph of wind magnitudes against time

% Plotting nrlmisse00 oxygen densities along Cubesat trajecotry
% for each day against time. Takes all parameters from textfiles as well
% as F10.7 monthly average, F10.7 daily average and Ap index

%%% HWM winds speeds along the trajectory of the Cubesat

cd ("C:\Users\Rifat\OneDrive - University College London\Rifat's PC\UCL\Y4\Project\MATLAB\CorrectINMSdata"); %path
disp("Plotting hwm winds vs time for a chosen day along CubeSat directory")

% extracting data from textfiles
date = importdata(textfile,' ');
lon = date.data(:,1);
lat = date.data(:,2);
h = date.data(:,3)*1000;
days = day(datetime(date.textdata(:,1)), 'dayofyear');
time = seconds(duration(date.textdata(:,2),'InputFormat','hh:mm:ss.SSSSSS','Format','hh:mm:ss.SSSSSS'));
api = repmat(ap,length(h),1);

% running HWM model
wind_model = atmoshwm(lon,lat,h,"day",days, "seconds", time,'apindex', api,'model','total','version','l4');
%mag_wind = sqrt((wind_model(:,1)).^2 + (wind_model(:,2)).^2);

% plotting routine
wind_vs_time = scatter(time,wind_model(:,2),"ro")
%wind_vs_time = quiver(wind_model(1:835,2),wind_model(1:835,1));
ylabel("HWM winds speeds (m/s)");
xlabel("time (s)");
grid on;
title(textfile)
legend(strcat("Ap index:",num2str(ap)))
end
|
```

Code snippet of the HWM subplots shown in figure 21

```
%%% plotting the magnitude of the wind speeds along the cubesat path

%% initialising figure
figure;
graph = tiledlayout(2,9);
title(graph,'Magnitude of HWM winds vs Time');

% day side

ax1 = nexttile;
[wind_vs_time] = hwm_alongpath_time("2018-5-19.txt",2)
ax2 = nexttile;
[wind_vs_time] = hwm_alongpath_time("2018-5-21.txt",2)
ax3 = nexttile;
[wind_vs_time] = hwm_alongpath_time("2018-5-22.txt",4)
ax4 = nexttile;
[wind_vs_time] = hwm_alongpath_time("2018-5-23.txt",8)
ax5 = nexttile;
[wind_vs_time] = hwm_alongpath_time("2018-5-25.txt",3)
ax6 = nexttile;
[wind_vs_time] = hwm_alongpath_time("2018-5-26.txt",3)
ax7 = nexttile;
[wind_vs_time] = hwm_alongpath_time("2018-5-27.txt",3)
ax8 = nexttile;
[wind_vs_time] = hwm_alongpath_time("2018-5-28.txt",4)
ax9 = nexttile;
[wind_vs_time] = hwm_alongpath_time("2018-5-29.txt",3)

% night side

ax10 = nexttile;
[wind_vs_time] = hwm_alongpath_time("2018-6-12.txt",3)
ax11 = nexttile;
[wind_vs_time] = hwm_alongpath_time("2018-6-13.txt",4)
ax12 = nexttile;
[wind_vs_time] = hwm_alongpath_time("2018-6-20.txt",5)
ax13 = nexttile;
[wind_vs_time] = hwm_alongpath_time("2018-6-23.txt",18)
ax14 = nexttile;
[wind_vs_time] = hwm_alongpath_time("2018-6-24.txt",6)
ax15 = nexttile;
[wind_vs_time] = hwm_alongpath_time("2018-6-25.txt",12)
ax16 = nexttile;
[wind_vs_time] = hwm_alongpath_time("2018-5-26.txt",20)
ax17 = nexttile;
[wind_vs_time] = hwm_alongpath_time("2018-6-28.txt",5)
ax18 = nexttile;
[wind_vs_time] = hwm_alongpath_time("2018-7-1.txt",2)

%%% same scale between all subplots
linkaxes([ax1 ax2 ax3 ax4 ax5 ax6 ax7 ax8 ax9 ax10 ax11 ax12 ax13 ax14 ax15 ax16 ax17 ax18], "y")
hold off
```

## A.6 MATLAB Code for HWM Vector Fields overlaid on NRLMSISE Contour Maps

This is a MATLAB function that reads the INMS textfiles and given Ap and f10.7 indices computes the HWM vector field overlaid on to a NRLMSISE density contour maps for a given day.

```

function [contour_vector] = densityANDwind(textfile, f107A, f107D, ap)

% HWM vector field overlaid on top of a NRLMSISE O density contour map.
% This will display arrows showing wind vector fields calculated by the HWM
% model and it will be plotted on top of the NRLMSISE oxygen density
% contour maps. The inputs for the function are the parameters from the
% textfiles, f10.7 values and Ap index.

%%% NOTE:
%%% This function will work only if "densityANDwind.m" file is in the same
%%% directory as the INMS textfiles. The function also depends on the
%%% HWM_vectorfield function. Please make sure "HWM_vectorfield.m" is also
%%% in the same directory as the INMS textfiles.

% changing directory to the directory where INMS textfiles are stored
%cd ("C:\Users\Rifat\OneDrive - University College London\Rifat's PC\UCL\Y4\Project\MATLAB\CorrectINMSdata"); %path
disp("Plotting HWM wind vector and NRLMSISE density contour map for each day")

% exporting data from textfiles
date = importdata(textfile,' ');
lon = date.data(:,1);
lat = date.data(:,2);
h = mean(date.data(:,3)*1000);
days = day(datetime(date.textdata(1,1), 'dayofyear');
time = seconds(duration(date.textdata(600,2),'InputFormat','hh:mm:ss.SSSSSS','Format','hh:mm:ss.SSSSSS'));
api = ap; %Ap value

% filling empty matrix with O density values
lat5 = [1:180];
lon5 = [1:360];
odens = nan(180,360);
for i = lat5
    for j = lon5
        [T, rho] = atmosnrlmsise00(h,i-91,j-181,2018,days,time,f107A,f107D,api); % Computing NRLMSISE model
        Ox = rho(:,2); % choosing O+ density from the list of outputs of the model
        odens(i,j) = Ox; %O+ density
    end
end

% plotting routine
load coastlines.mat;
[X,Y]= meshgrid(-179:180, -89:90);
contourf(X,Y,odens,100,"LineColor","none")
colorbar
hold on;
plot(coastlon, coastlat,"b")
box on
xlim([-180 180])
ylim([-90 90])
xlabel("longitude")
ylabel("latitude")
hold on
[contour_vector] = HWM_vectorfield(textfile,3)
hold off

end

```

## A.7 Calculations of Angle Between HWM Vectors and INMS's Look Direction

This MATLAB snippet shows the calculations that were performed in order to find the angle between the INMS look direction and the HWM horizontal wind vector at the high geometric factor peak's location.

```
%%% calculations to investigate the direction of the wind vectors %%%

disp("Calculations to investigate the direction of the wind vectors with respect to INMS")

% 29th of May
disp("29th of May")
w29 % HWM wind vector at high geometric factor peak's location and time
norm(w29)
atand(w29(1)/w29(2)) % finding the angle between the HWM vector components
y = -47.82 - -49.18
x = -55.98 - -50.69
atand(y/x) % finding the angle of the INMS's look direction
disp("Angle between INMS look direction and wind vector field")
atand(w29(1)/w29(2)) - atand(y/x) % difference between the HWM direction and INMS look direction
%not in field of view

% 28th of May
disp("28th of May")
w28
norm(w28j)
atand(w28(1)/w28(2))
y = -49.48 - -50.48
x = -59.43 - -53.80
atand(y/x)
disp("Angle between INMS look direction and wind vector field")
atand(w28(1)/w28(2)) - atand(y/x) %not in field of view

% 27th of May
disp("27th of May")
w27
norm(w27)
atand(w27(1)/w27(2))
y = -48.20 - -49.49
x = -51.57 - -46.20
atand(y/x)
disp("Angle between INMS look direction and wind vector field")
atand(w27(1)/w27(2)) - atand(y/x) %not in field of view

% 26th of May
disp("26th of May")
w26
norm(w26)
atand(w26(1)/w26(2))
y = -50.72 - -51.32
x = -48.98 - -43.08
atand(y/x)
disp("Angle between INMS look direction and wind vector field")
atand(w26(1)/w26(2)) - atand(y/x) %not in field of view
```

## A.8 Final Calculation of Calibration Factor and Neutral Wind Speed

This MATLAB snippet shows the calculations that were performed in order to find the final calibration factor  $f$  and the neutral wind speed  $w$ .

```
%%% Final calculations to find calibration factor f and neutral wind speed %%%

mean(peak_shifts) % average of peak shifts
mean(N(1:33)) % average of high geometric factor INMS counts
mean(Ne(1:33)) % average of IRI O+ number densities
HWHw = mean([norm(w26),norm(w27),norm(w28),norm(w29)]) % average of HWHw winds
cf = (mean(Ne(1:33))/mean(N(1:33)))*(HWHw + 7730)*(1.37*10^(-6)) % calibration factor
w = ((1.45*10^-9)*cf/(1.37*10^-6)-7730)*(1/cosd(mean(peak_shifts))) % neutral wind speed

ans = -4.0952
ans = 874.8788
ans = 7.8084e+10
HWHw = 112.9690
cf = 9.5899e+05
w = -6.7322e+03
```

## A.9 Pitch Angle Distribution

Distribution of Pitch Angles from different dates shown below.

